Supplementary Information

Electron delocalization-driven high dielectric electrolyte for solid-state lithium metal batteries

Xufei An[1,2,+], Ke Yang[1,2,+], Likun Chen[1,*], Jinshuo Mi[1,2], Guanyou Xiao[1,2], Wenting Cui[1,2], Yuetao Ma[1,2], Shaoke Guo[1,2], Yuhang Li[1,2], Zhuo Han[1,2], Peiran Shi[1], Ming Liu[1], Dan Li[3], Feiyu Kang[1,2] and Yan-Bing He[1,*]

[1] Shenzhen All-Solid-State Lithium Battery Electrolyte Engineering Research Center, Institute of Materials Research (IMR), Tsinghua Shenzhen International Graduate School, Tsinghua University, Shenzhen 518055, China.

[2] School of Materials Science and Engineering, Tsinghua University, Beijing 100084, China.

[3] Department of Chemical and Biological Engineering, The Hong Kong University of Science and Technology, Clear Water Bay, Kowloon, Hong Kong

[+] These authors contributed equally: Xufei An, Ke Yang.

Correspondence and requests for materials should be addressed to L. C. (email: chenlikun1997@gmail.com) or Y.-B. H. (email: he.yanbing@sz.tsinghua.edu.cn)

Table of Contents

Supplementary Figures

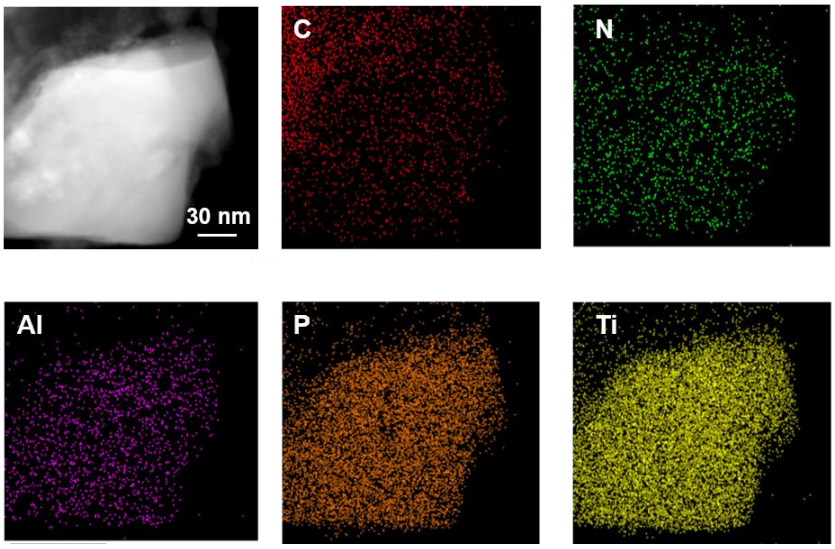

Supplementary Fig. 1 HAADF-STEM image and EDS mappings of LATP@d-PANI

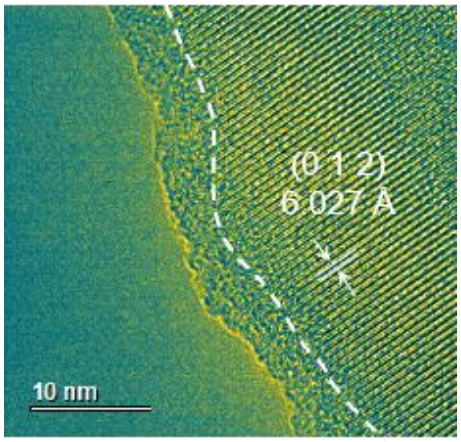

Supplementary Fig. 2 TEM image of LATP@d-PANI

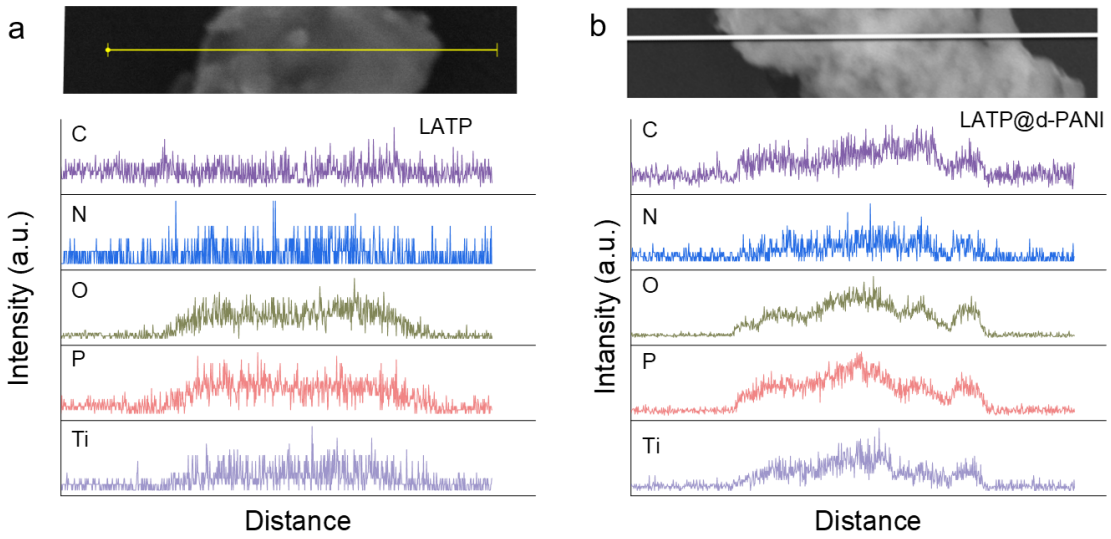

Supplementary Fig. 3 EDS line-scanning analysis of (a) LATP and (b) LATP@d-PANI

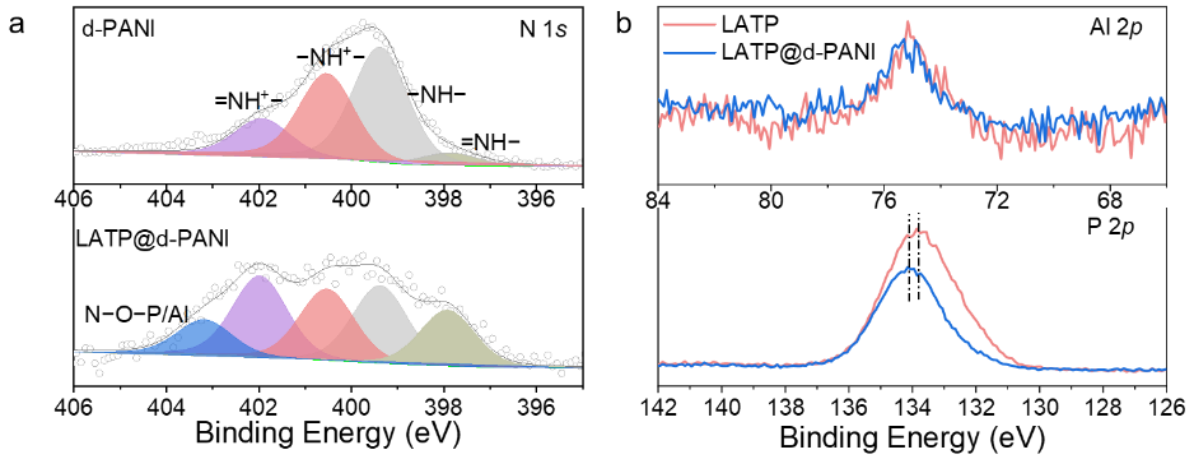

Supplementary Fig. 4 (a) XPS spectra of N 1*s* in d-PANI and LATP@d-PANI; (b) XPS spectra of Al 2*p* and P 2*p* in LATP and LATP@d-PANI

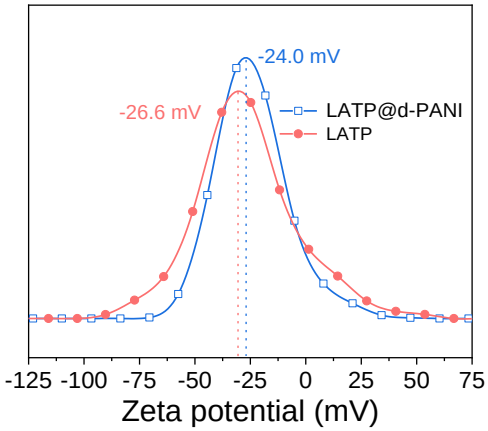

Supplementary Fig. 5 Zeta potential distribution data of LATP and LATP@d-PANI

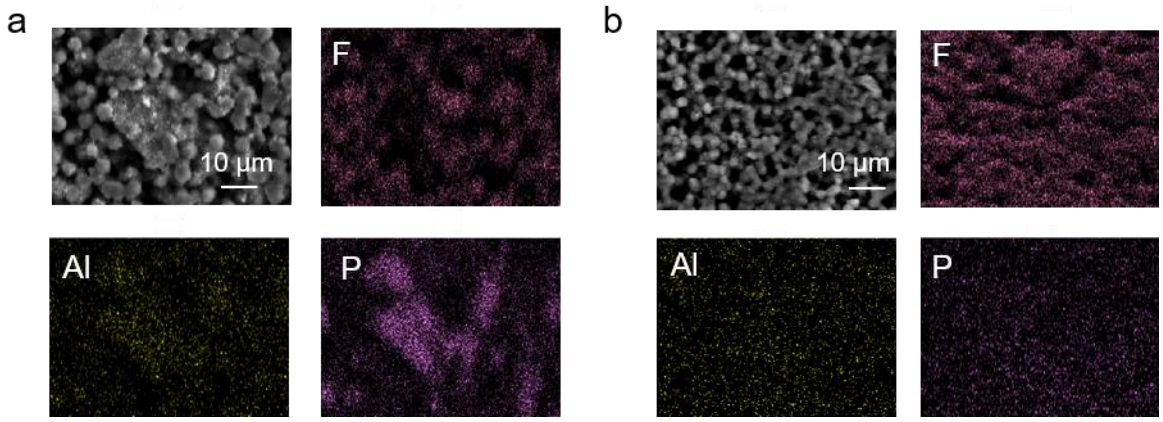

Supplementary Fig. 6 SEM images and the corresponding EDS mapping of the PVPL electrolyte (a) and PLPA electrolyte (b)

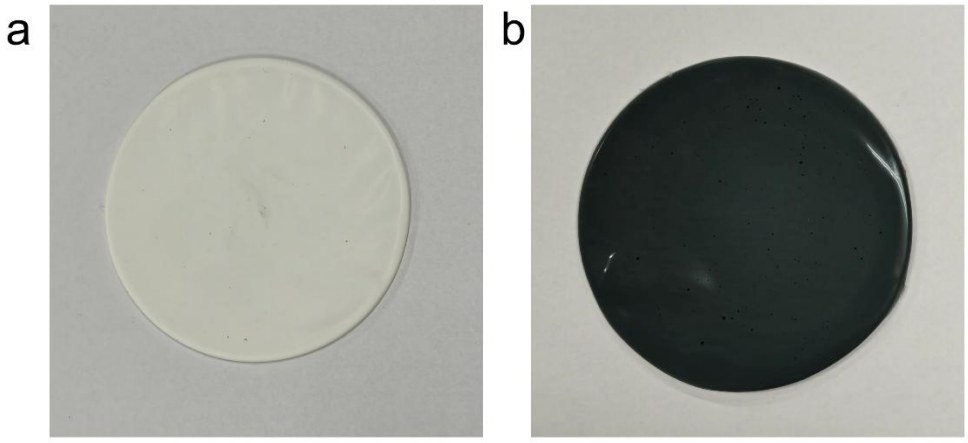

Supplementary Fig. 7 Optical photographs of the PVPL electrolyte (a) and PLPA electrolyte (b)

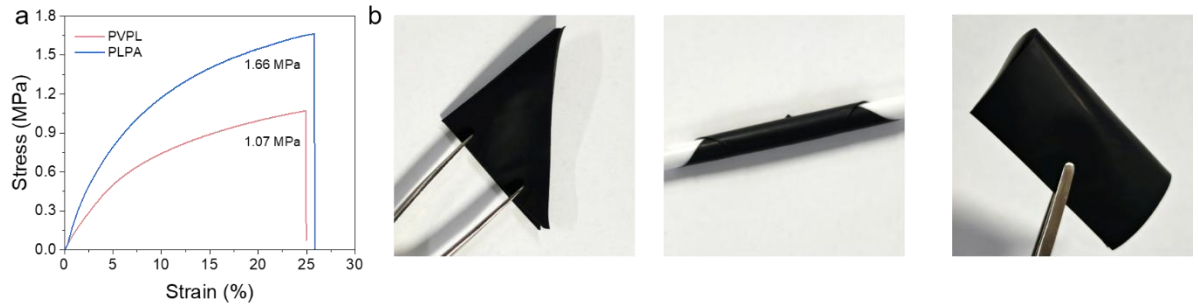

Supplementary Fig. 8 (a) Stress-strain curves of the PVPL and PLPA electrolytes; (b) Optical photographs of the PLPA electrolyte can be folded and wound

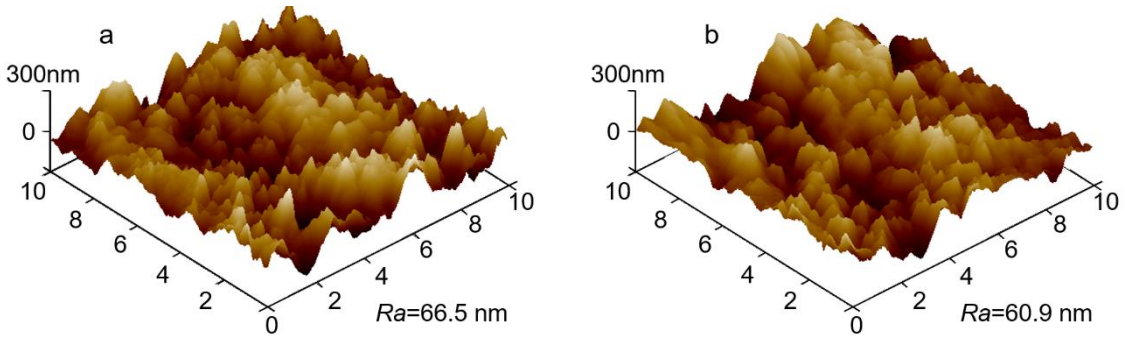

Supplementary Fig. 9 AFM topography of (a) PVPL and (b) PLPA electrolytes

Supplementary Note 1 | Characterization of electrolytes

The incorporation of $Li_{1.4}Al_{0.4}Ti_{1.6}(PO_4)_3$ (LATP) into PVDF electrolytes can enhance their mechanical strength and chemical stability[1,2]. Therefore, 15 wt% LATP was incorporated into PVDF-LiFSI electrolyte to obtain composite solid electrolyte (PVPL). The LATP@d-PANI was synthesized through ball-milling d-PANI and LATP at a specific mass ratio to take advantage of the compatibility of d-PANI with PVDF, which enables a more uniform distribution of LATP within the electrolyte. High-angle annular dark-field scanning transmission electron microscopy (HAADF-STEM) together with energy-dispersive spectroscopy (EDS) mapping (**Supplementary Fig. 1**) and TEM images (**Supplementary Fig. 2**) affirm a consistent coating of approximately 4 nm thickness of d-PANI on the surfaces of LATP particles. The EDS line-scanning profiles also demonstrate that C and N elements are distributed on the LATP surface following the ball-milling process (**Supplementary Fig. 3**), suggesting a robust coupling between d-PANI and LATP. Moreover, the N 1*s* XPS spectra of the LATP@d-PANI composite exhibit characteristic d-PANI signals along with a distinct new peak at 403.18 eV, corresponding to the formation of N–O–P/Al bonding[3,4]. The chemical interaction between LATP and d-PANI is also substantiated by the binding energy shifts observed in the P 2*p* and Al 2*p* XPS spectra (**Supplementary Fig. 4**), indicating the presence of a strong interaction between the d-PANI and LATP surfaces. In **Supplementary Fig. 5**, the zeta potential of LATP@d-PANI particles exhibits a slight reduction, measuring at −24.0 mV, in contrast with the −26.6 mV zeta potential observed for pristine LATP particles. These results portend high dispersion of LATP@d-PANI particles in slurry, laying the foundation for synthesizing homogenized polymer electrolyte composite (PLPA) without ceramic aggregation. To evaluate the dispersion of LATP@d-PANI in PVDF electrolytes, a certain amount of LATP@d-PANI was incorporated into PVDF-LiFSI electrolyte to obtain the PLPA electrolyte. As shown in **Supplementary Fig. 6**, the LATP exhibits obvious aggregation in the PVPL electrolyte, while in the PLPA electrolyte, LATP@d-PANI is uniformly distributed throughout the electrolyte. As a result, the PLPA electrolyte shows a much denser structure and less surface roughness than the PVPL electrolyte, improving the mechanical property of the PLPA electrolyte (**Supplementary Figs. 7-9**). Additionally, the PLPA electrolyte can be folded and wound, demonstrating the excellent flexibility (**Supplementary Fig. 8b)**.

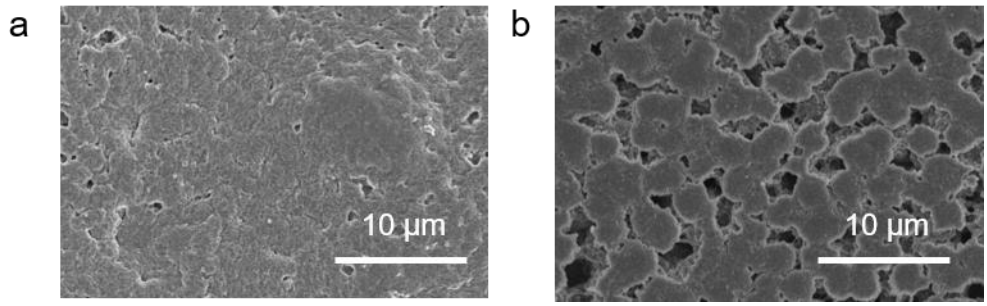

Supplementary Fig. 10 SEM images of the PLPA electrolyte (a) and PVPL electrolyte (b)

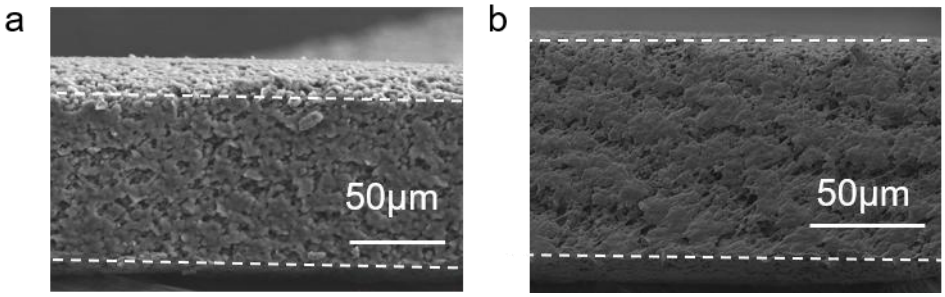

Supplementary Fig. 11 Cross-sectional SEM images of the PLPA (a) and PVPL (b) electrolytes

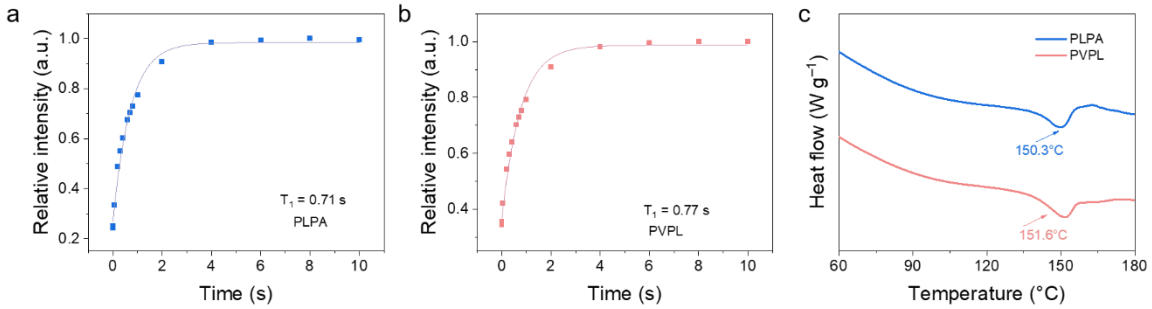

106

107 **Supplementary Fig. 12** The spin–lattice relaxation rate (T_1) of ^{19}F in the PVDF of the (a) PLPA

108 electrolyte and (b) PVPL electrolyte; (c) DSC curves of PLPA electrolyte and PVPL electrolyte

109 The differential scanning calorimetry (DSC) and the solid-state nuclear magnetic resonance (ss-NMR)

110 of ^{19}F were performed to investigate the dynamics/relaxation of polymers. The DSC curves display

111 that the melting temperature (T_m) of PVPL and PLPA electrolytes is 151.6 and 150.3℃, respectively,

112 exhibiting negligible change (Supplementary Fig. 12). The spin–lattice relaxation rate of ^{19}F in PVDF

113 (T_1) of the PVPL and PLPA electrolytes shows no significant changes. These findings indicate that

114 the introduction of d-PANI does not markedly affect PVDF polymer dynamics.

115

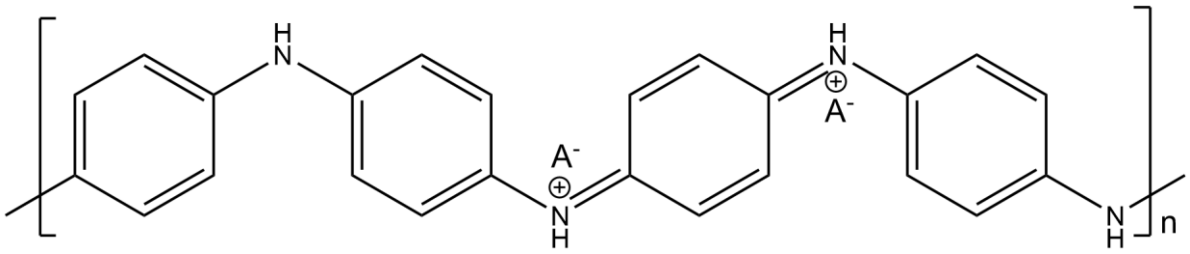

Supplementary Fig. 13 Molecular structure of d-PANI (A^- is the anion of the doped acid)

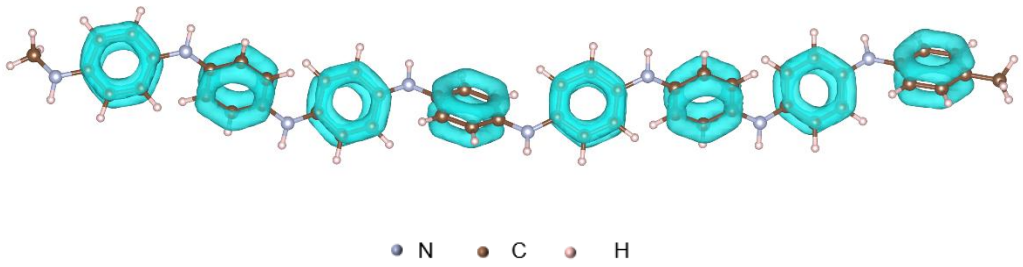

Supplementary Fig. 14 The localized orbital locator-π (LOL-π) mappings of d-PANI

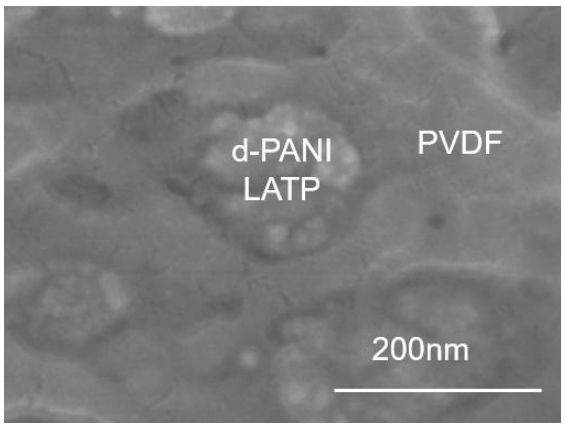

Supplementary Fig. 15 The cross-sectional SEM image of PLPA film

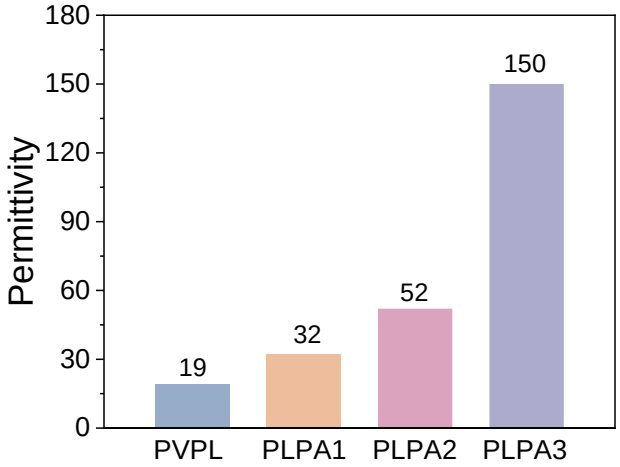

Supplementary Fig. 16 Dielectric constant of the PVPL and PLPA films with different amounts of d-PANI at 25 °C and 20 Hz

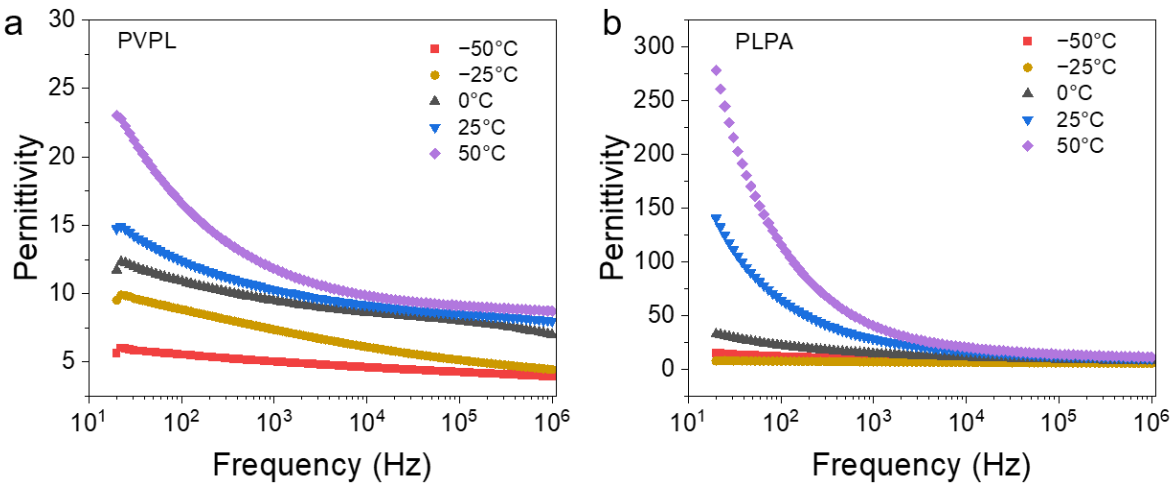

Supplementary Fig. 17 Dielectric constant of (a) PVPL and (b) PLPA films at different temperature

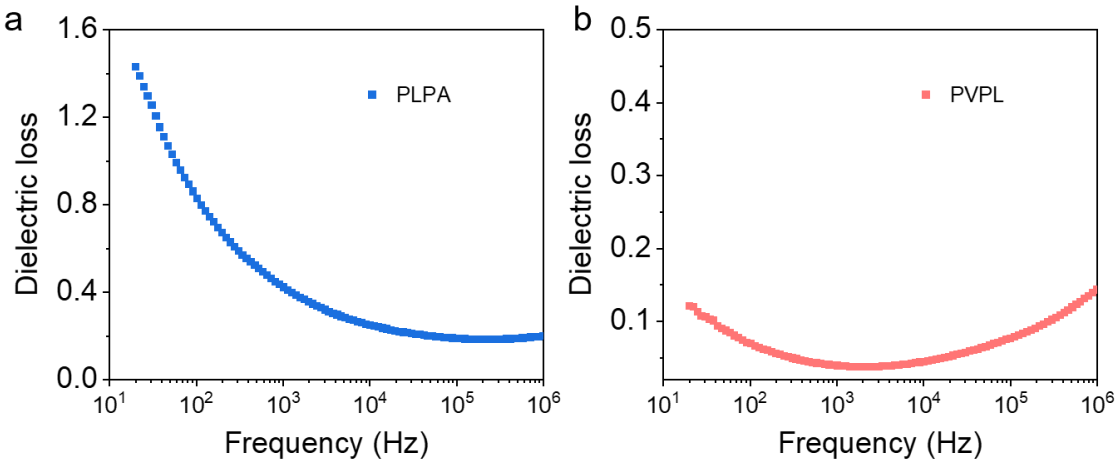

Supplementary Fig. 18 Dielectric loss tangent of (a) PLPA and (b) PVPL films

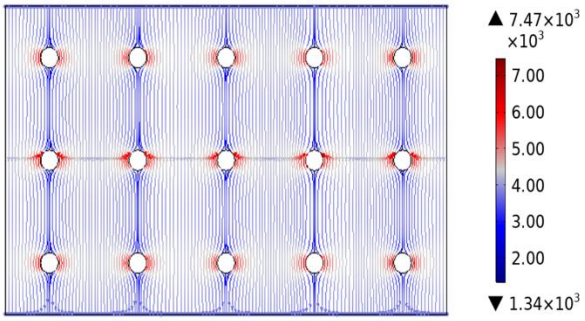

Supplementary Fig. 19 Finite element simulation of the current density in the PLPA electrolyte

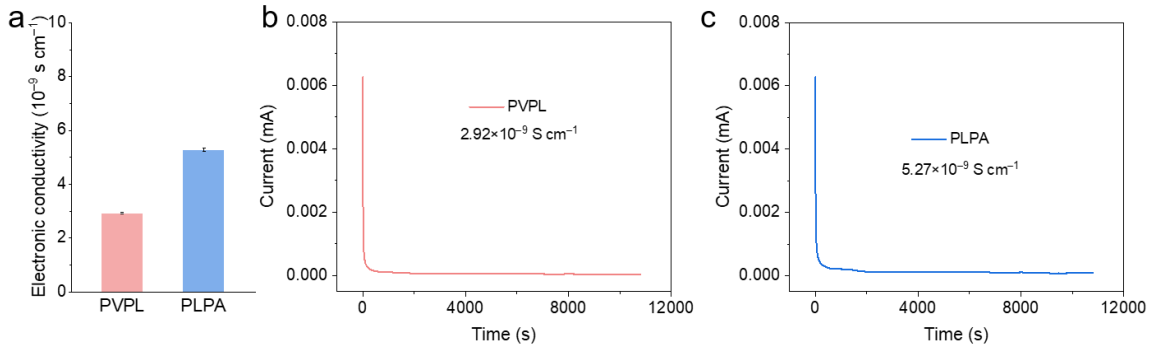

Supplementary Fig. 20 (a) The electronic conductivity of PVPL and PLPA electrolytes (Data were analyzed from more than three experiments); Current-time curves of symmetric cells with stainless steel as electrodes for the electronic conductivity of (b) PVPL and (c) PLPA electrolytes

To investigate the influence of d-PANI on electronic conductivity of the composite electrolyte, the symmetric cells with stainless steel as electrodes were assembled and conducted Chronoamperometry (CA) tests with applied voltage of 1 V. The results show that the electronic conductivity of PVPL and PLPA electrolytes is 2.92×10^{-9} S cm^{-1}and 5.27×10^{-9} S cm^{-1}, respectively, as shown in **Supplementary Fig. 20**.

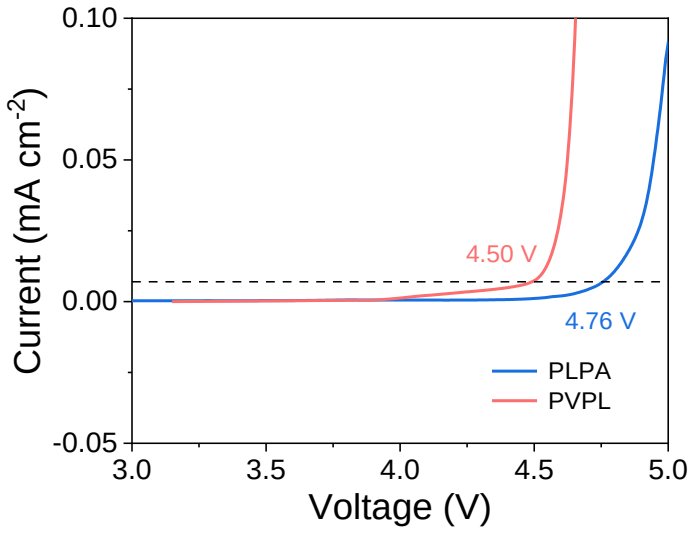

Supplementary Fig. 21 Linear sweep voltammetry (LSV) curves of the PVPL and PLPA electrolytes

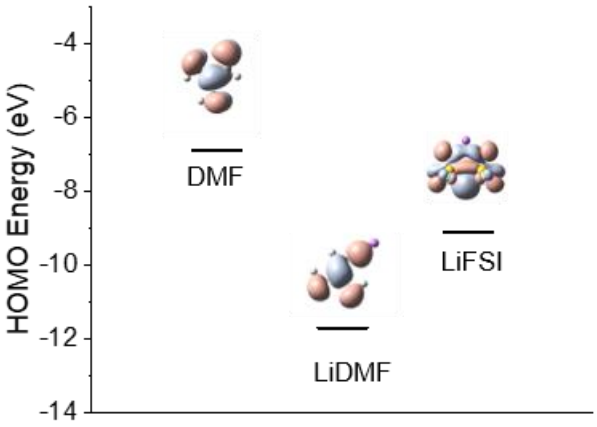

Supplementary Fig. 22 HOMO energy of DMF, LiDMF and LiFSI

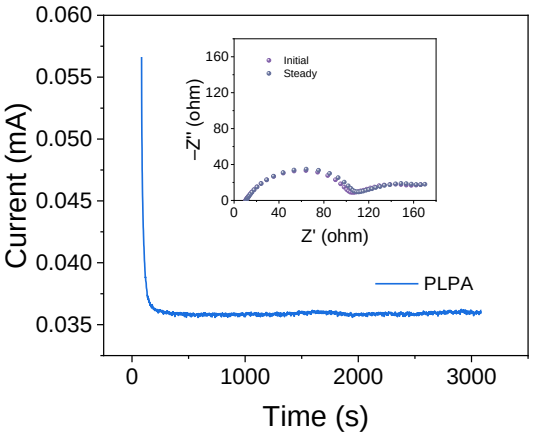

Supplementary Fig. 23 The Li-ion transference number of PLPA electrolyte

Supplementary Note 2| Dissociation kinetics of Li salts

Herein, the dissociation kinetics of Li salts is characterized by a specific ionic conductance of $G_{\Delta E}$, which includes the contributions from the (1) intrinsic Li^+ conductance of SPEs without an electric field ($G_0 = 1/R_0$) and (2) the enhanced Li^+ conductance of SPEs after applying an electric field. The second item can be determined by $\Delta E \cdot G_E$, where G_E (S V^{-1}) is the Li^+ conductance per unit voltage. Therefore, a linear relationship between $G_{\Delta E}$ and ΔE can be established as $G_{\Delta E} = G_E \Delta E + G_0$. The $G_{\Delta E}$ values are determined by measuring the Li^+ conductance of electrolytes under the corresponding ΔE.

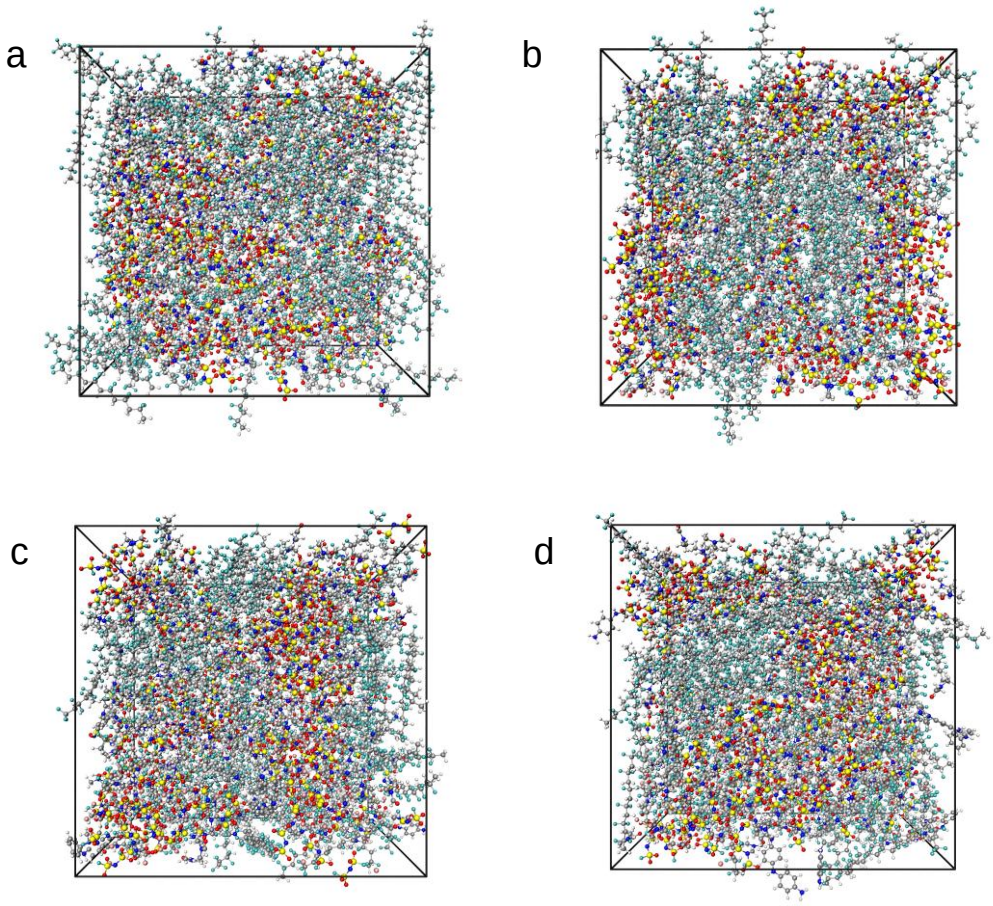

Supplementary Fig. 24 The snapshot of MD simulations for the PVPL electrolyte (a) and PVPL electrolyte with electric field (b); the PLPA electrolyte (c) and PLPA electrolyte with electric field (d)

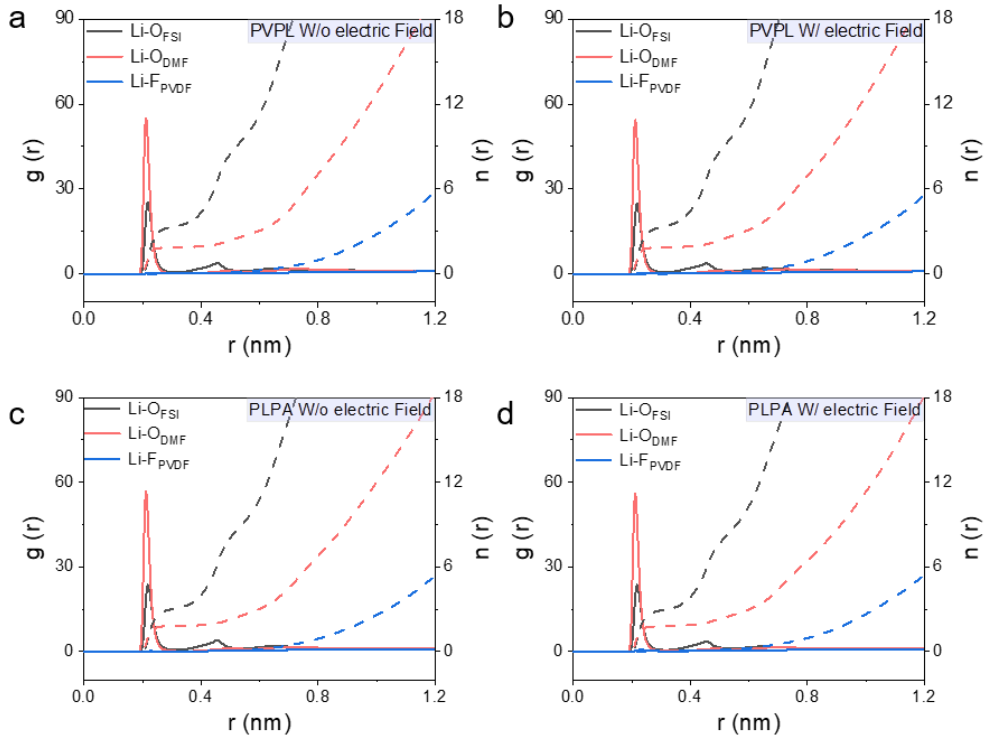

175

176 **Supplementary Fig. 25** Radial distribution functions (RDF) and coordination number obtained by
177 molecular dynamics (MD) simulations in the PVPL electrolyte without (a) and with (b) electric field;
178 the PLPA electrolyte without (c) and with (d) electric field

179

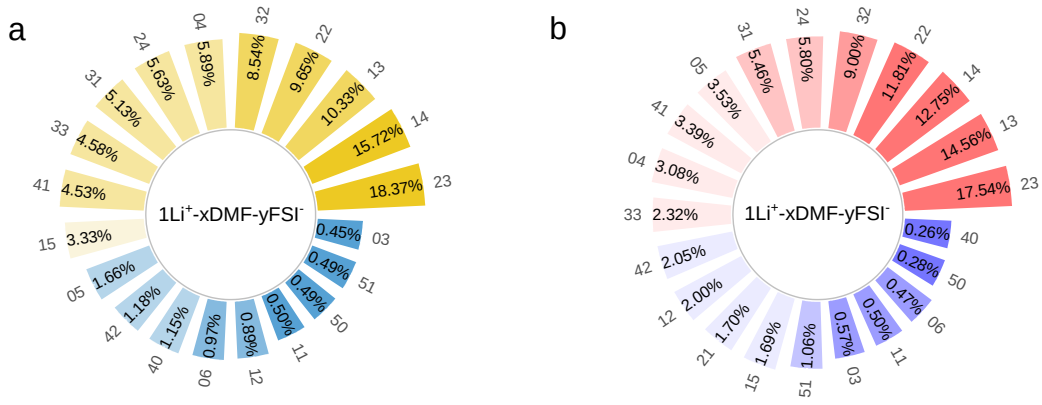

180

181 **Supplementary Fig. 26** Proportion of probable coordination structures from MD simulations in the

182 PVPL electrolyte with (a) and without (b) electric field

183 The **Supplementary Fig. 26** exhibits a negligible change in the proportion of high coordination

184 numbers of FSI^- with Li^+ for the PVPL electrolyte under electric field, which is consistent with the

185 coordination number of FSI^- with Li^+ (Li–O (FSI^-) and Li–N (FSI^-)) of the PVPL electrolyte under

186 electric field.

187

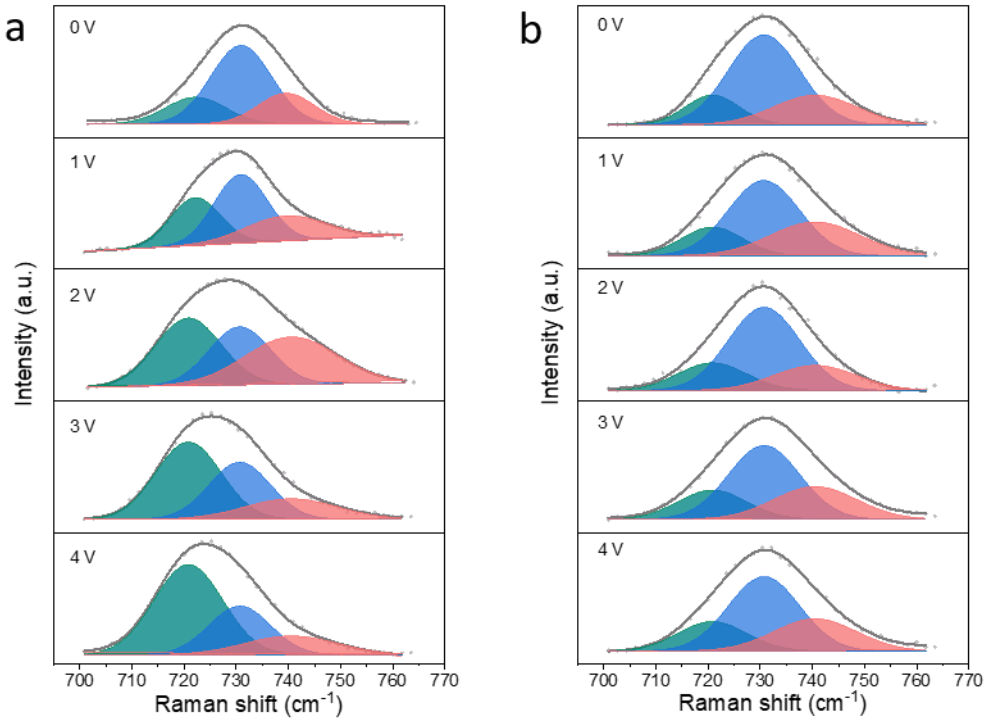

Supplementary Fig. 27 Raman spectra of the PLPA electrolyte (a) and PVPL electrolyte (b) and corresponding quantification results of the FSI^- anion states in the electrolytes under different voltages

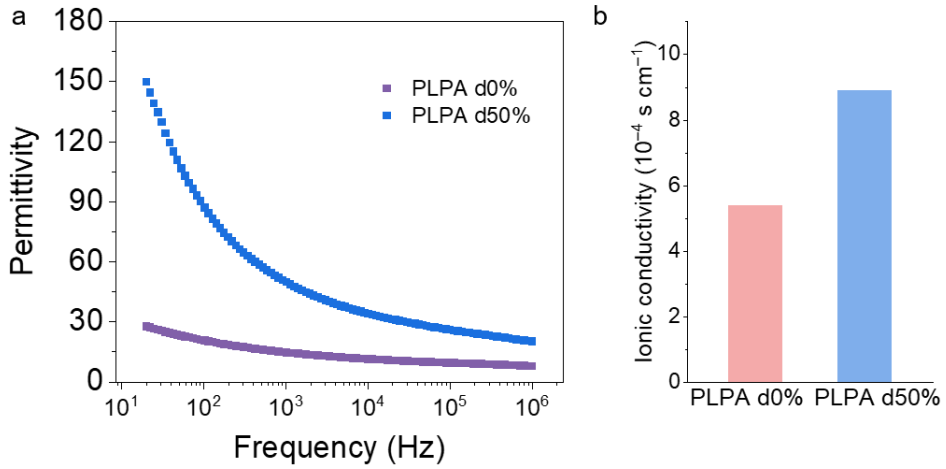

Supplementary Fig. 28 (a) The dielectric constant of films containing undoped PANI (0% doping) and 50%-doped PANI (the d-PANI used in this work); (b) ionic conductivity of the electrolyte containing undoped PANI (0% doping) and 50%-doped PANI (the d-PANI used in this work)

As shown in **Supplementary Fig. 28**, at a fixed loading of 3 wt%, the ionic conductivity of electrolytes and dielectric constant of the films containing undoped PANI (0% doping) are significantly lower than that with 50%-doped PANI (the d-PANI used in this work). This indicates that the "micro-capacitors" induced by electron delocalization of d-PANI effectively promote Li salt dissociation and ion transport in PLPA electrolyte.

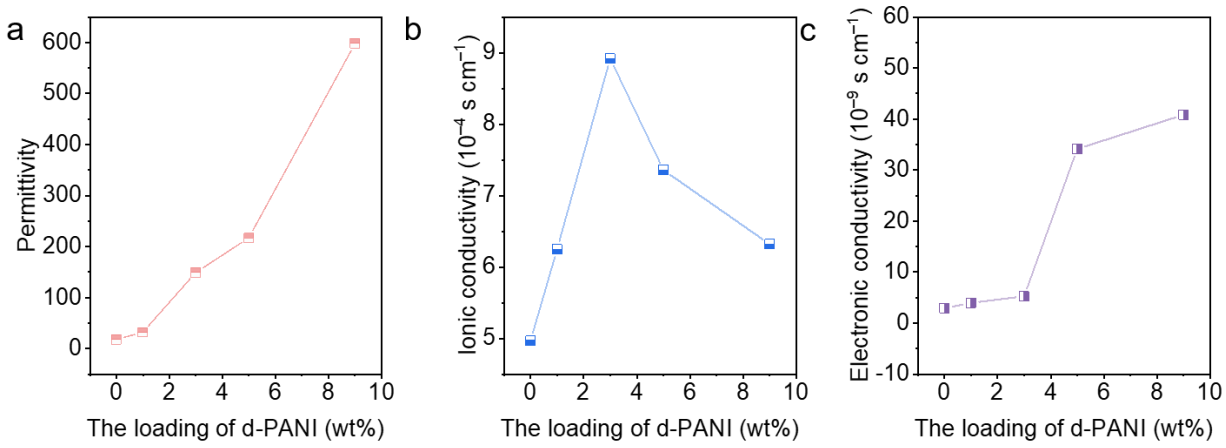

Supplementary Fig. 29 The evolution of dielectric constant (a), ionic conductivity (b) and electronic conductivity (c) varies with the change of d-PANI loading amount

Meanwhile, the **Supplementary Fig. 29** presents both the ionic and electronic conductivities of electrolytes with varying d-PANI loadings. When the loading exceeds 3 wt%, a pronounced increase in electronic conductivity is observed, whereas the enhancement in ionic conductivity becomes marginal. This can be attributed to the aggregation of d-PANI particles at higher loadings, which compromises their isolated distribution and thus weakens the “micro-capacitor” effect. Therefore, in this work, a d-PANI loading of 3 wt% was selected to ensure efficient ion transport while avoiding electronic leakage.

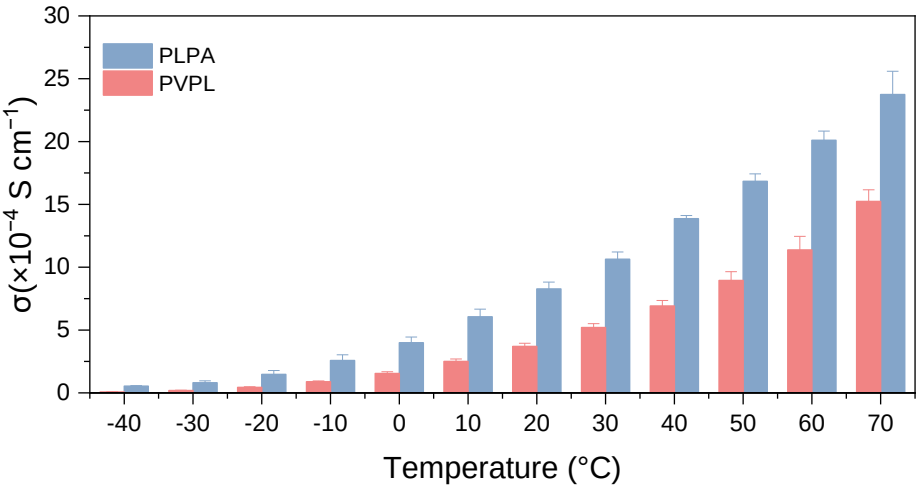

214

215 **Supplementary Fig. 30** The ionic conductivity of the PLPA electrolyte and PVPL electrolyte at

216 various temperature (Data were analyzed from more than three experiments)

217

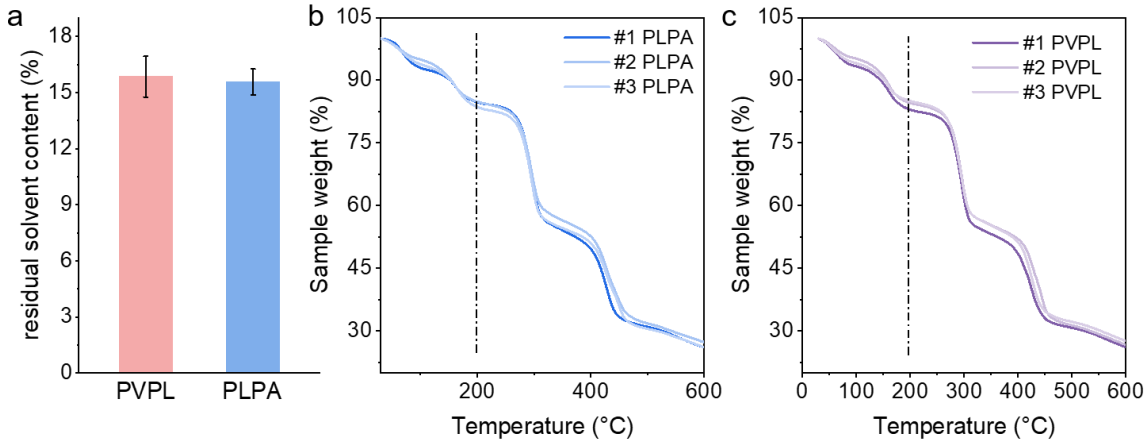

Supplementary Fig. 31 (a)The residual solvent content in PVPL electrolyte and PLPA electrolyte (Data were analyzed from more than three experiments); TGA curves of (b) PLPA electrolyte and (c) PVPL electrolyte

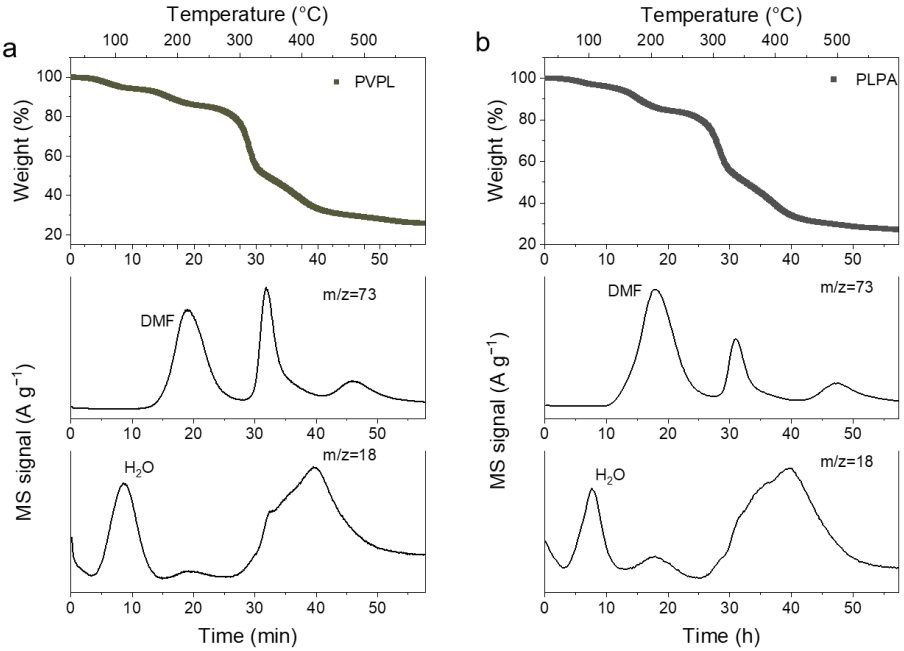

223

224 **Supplementary Fig. 32** TG-MS curves of (a) PVPL electrolyte and (b) PLPA electrolyte

225

226

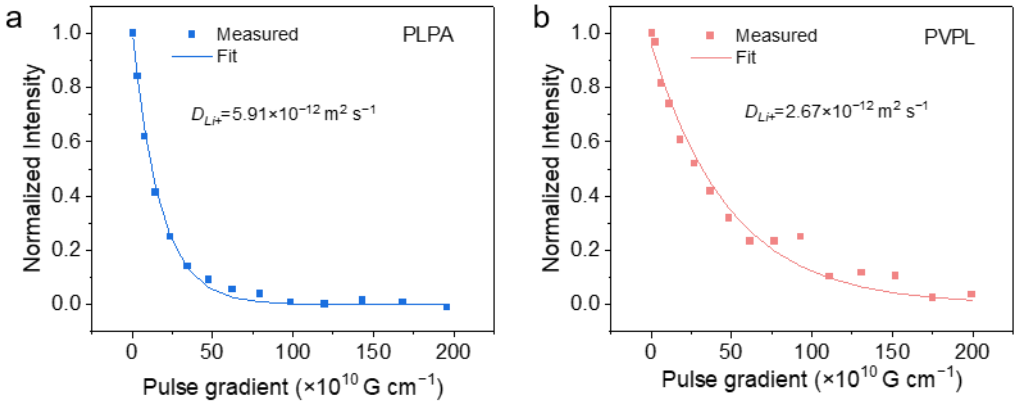

227

228 **Supplementary Fig. 33** Li^+ diffusion coefficient of (a) PLPA electrolyte and (b) PVPL electrolyte

229 tested by PFG-NMR

230

Supplementary Note 3| The influence of electrolyte microstructure on ion transport

To further investigate the influence of electrolyte microstructure on Li^+ transport, the dense PVPL electrolyte (denoted as dense-PVPL) by vacuum oven drying, which is a modified fabrication method derived from the original PVPL electrolyte. And a relatively porous PLPA electrolyte (denoted as porous-PLPA) by increasing the ratio of solvent, which is a modified fabrication method derived from the original PLPA electrolyte (**Supplementary Fig. 34**). To clarify how the denser morphology affects the distribution of the residual solvent and the Li^+ transport pathways, the atomic force microscope-nano-infrared (AFM-nano-IR) map was performed to elucidate the distribution of residual solvent (DMF) in the electrolytes. As shown in **Supplementary Fig. 35**, **36**, the DMF is locally aggregated inside the bulk of the PVDF spherulites rather than in the pores. Therefore, the denser structure of PVDF-based electrolytes would promote the uniform distribution of DMF, which could potentially contribute to uniform and abundant Li^+ transport pathways. However, the influence of morphology alone on ionic conductivity appears to be limited. The dense-PVPL electrolyte exhibits an ionic conductivity of 5.01×10^{-4} S cm^{-1} (**Supplementary Fig. 37a**), which is close to that of the PVPL electrolyte, indicating that the effect of ionic conductivity enhancement from electrolyte morphology is very limited. This is owing to the low population of dissociated and mobile Li^+ in the PVPL system. In contrast, the porous-PLPA electrolyte still exhibits a high ionic conductivity of 8.58×10^{-4} S cm^{-1}, comparable to that of the PLPA electrolyte. Taken together, these results indicate that although morphology can influence the distribution of residual DMF and the uniformity of ion-transport pathways, the markedly improved ionic conductivity of PLPA mainly arises from enhanced Li-salt dissociation induced by the strong dielectric response associated with the electron delocalization of d-PANI. Furthermore, the results of thermogravimetric analysis exclude the effect of the residual solvent content on ion transport (**Supplementary Fig. 37b, c**).

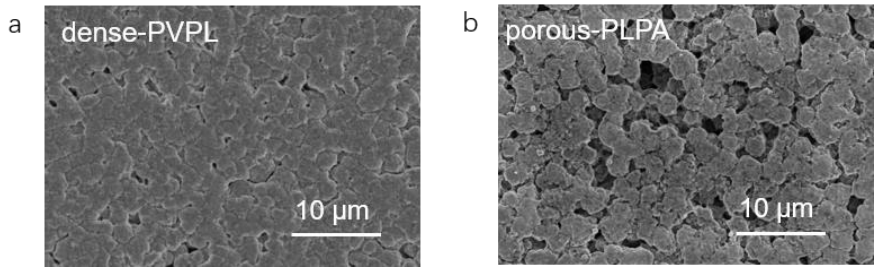

Supplementary Fig. 34 SEM images of (a) dense-PVPL electrolyte and (b) porous-PLPA electrolyte

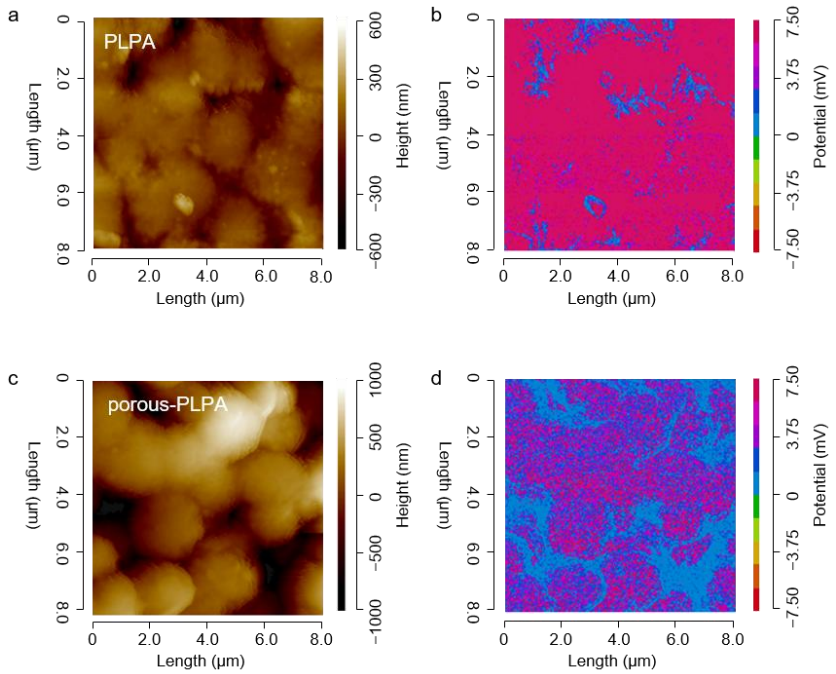

Supplementary Fig. 35 AFM image of the PLPA electrolyte (a) and porous-PLPA electrolyte (c) and corresponding nano-infrared overlap of the C=O vibration of DMF in the PLPA electrolyte (b) and porous-PLPA electrolyte (d) (the red areas indicate a stronger DMF absorption intensity)

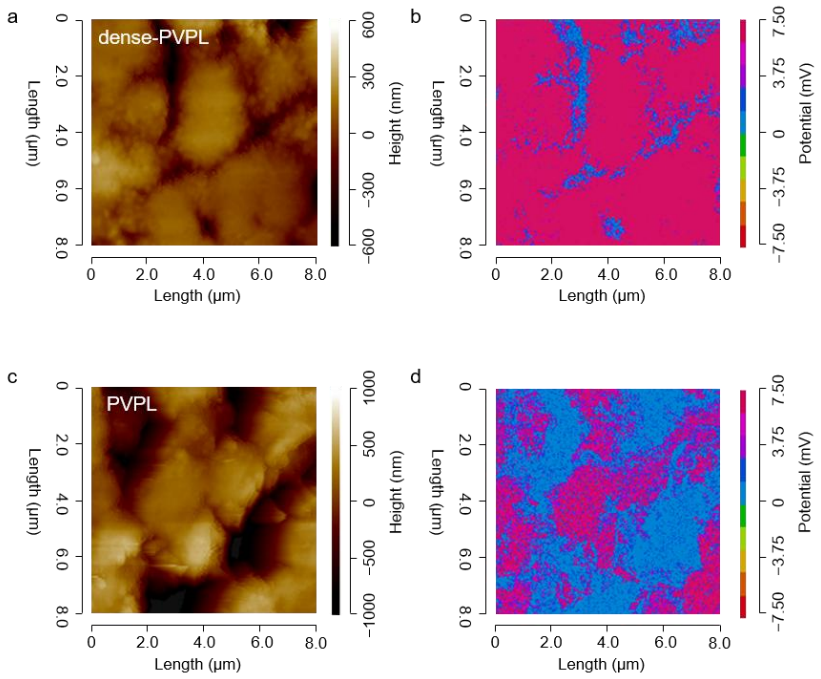

Supplementary Fig. 36 AFM image of the dense-PVPL electrolyte (a) and PVPL electrolyte (c) and corresponding nano-infrared overlap of the C=O vibration of DMF in the dense-PVPL electrolyte (b) and PVPL electrolyte (d) (the red areas indicate a stronger DMF absorption intensity)

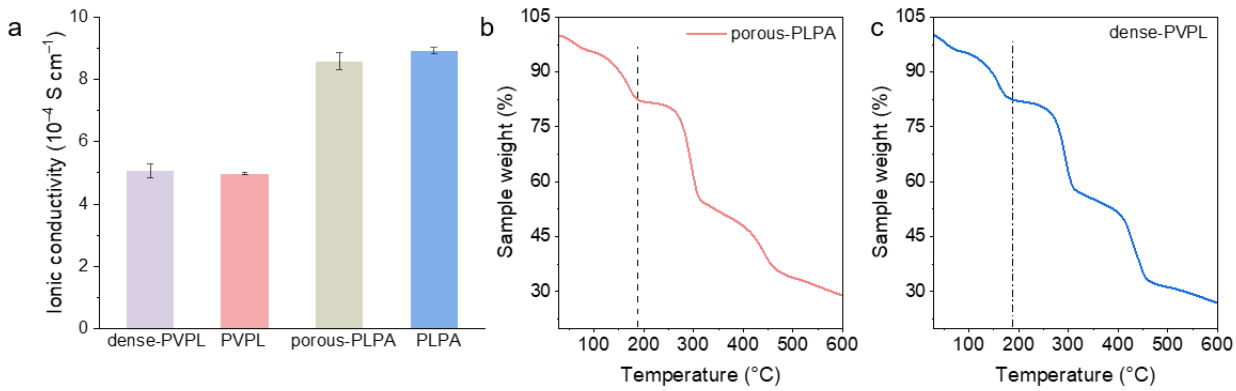

Supplementary Fig. 37 (a) The ionic conductivity of dense-PVPL, PVPL, porous-PLPA and PLPA electrolyte (Data were analyzed from more than three experiments); (b) TGA curves of porous-PLPA electrolyte; (c) TGA curves of dense-PVPL electrolyte

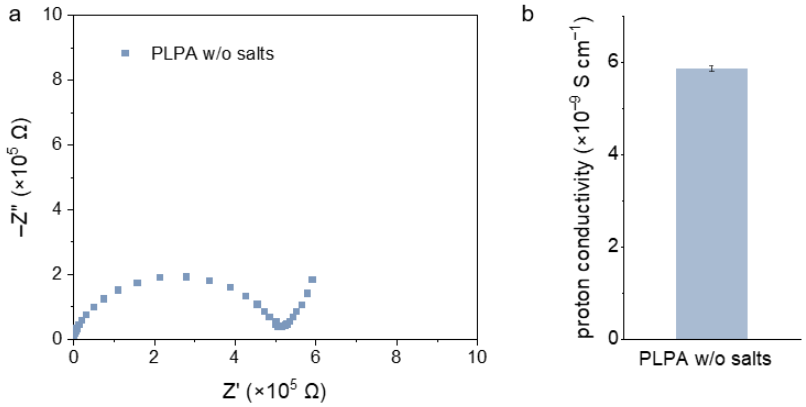

Supplementary Fig. 38 (a) Nyquist plots and fitted results of PLPA w/o salts; (b) The proton conductivity of PLPA w/o salts (Data were analyzed from more than three experiments)

To investigate the influence of proton conduction from d-PANI on the ionic conductivity enhancement, a sample of PLPA electrolyte that does not contain the Li salt (LiFSI) was prepared (denoted as PLPA w/o salts) to eliminate the influence of Li^+ conductivity. Its proton conductivity was measured by electrochemical impedance spectroscopy (EIS) from 7.00 MHz to 0.01 Hz with a 10 mV alternating current (AC) oscillation on a VMP3 multichannel electrochemical station (*Ind. Eng. Chem. Res. 44, 20, 7617–7626 (2005)*; *Nat Commun 15, 3930 (2024)*). The results show that their proton conductivity is 5.86×10^{-9} S cm^{-1} (**Supplementary Fig. 38**). These values are five orders of magnitude lower than the measured total ionic conductivity (10^{-4} S cm^{-1}) of PLPA electrolyte, confirming that the contribution of proton conductivity is negligible.

Supplementary Note 4| The versatility of the electron delocalization strategy

To assess the generality of ion-transport enhancement induced by the dielectric response from the electron delocalization of d-PANI, polymer electrolytes based on poly (ethylene oxide) (PEO) and polyacrylonitrile (PAN) systems were fabricated using the same fabrication method as employed for the PVDF system. First, the d-PANI was incorporated into PEO-LiFSI electrolyte with LATP filler (termed PEPL) to obtain a membrane of composite polymer electrolyte (termed PEPA). As shown in **Supplementary Fig. 39**, the PEPA electrolyte exhibits a much higher room-temperature ionic conductivity of 2.06×10^{-4} S cm^{-1} than that of PEPL electrolyte (0.69×10^{-4} S cm^{-1}), with a low activation energy (E_a) of 0.24 eV. It should be noted that the residual solvent content in both the PEPL and PEPA electrolytes is approximately 5 wt%. Furthermore, the free FSI^- of PEPA electrolyte increases from 26.8% for PEPL electrolyte to 55.1%, suggesting that d-PANI in the electrolyte promotes the dissociation of Li salt. Then, the d-PANI was incorporated into PAN-LiFSI electrolyte with LATP filler (termed PAPL) to obtain a composite polymer electrolyte (termed PAPA). Compared with the PAPL electrolyte (**Supplementary Fig. 40**), the PAPA electrolyte shows higher ionic conductivity (1.37×10^{-4} S cm^{-1}), lower E_a (0.30 eV), and a greater proportion of free FSI^-. These results are consistent with those observed in the PEO system, indicating that the enhancement of ionic conductivity by electron delocalization-induced dielectric response to promote Li salt dissociation, is effective across different polymer systems.

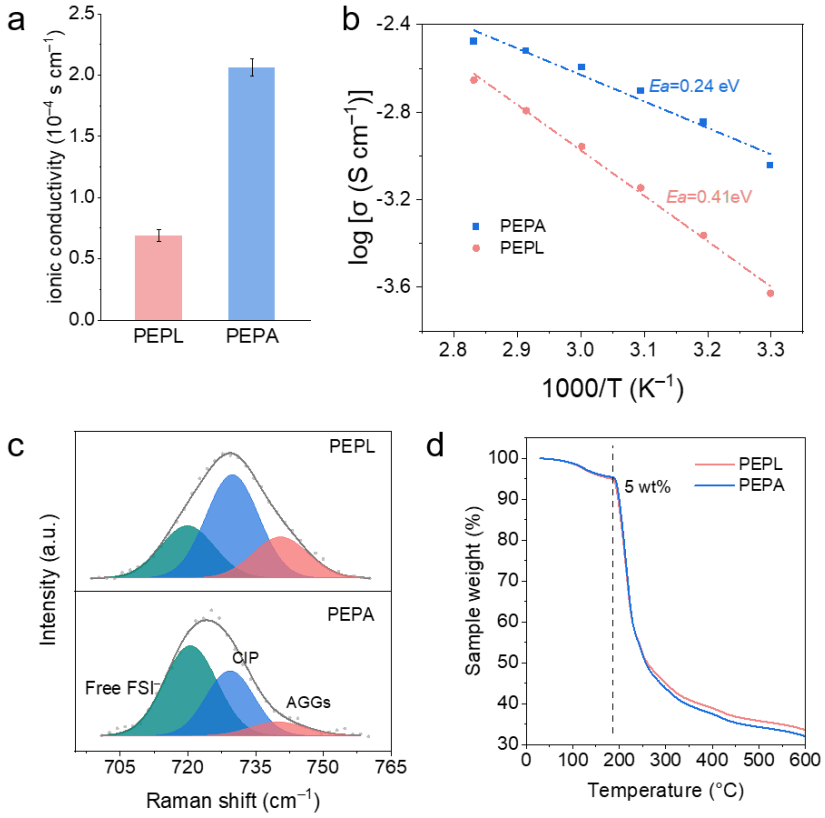

Supplementary Fig. 39 (a) The ionic conductivity of PEPL and PEPA electrolytes (Data were analyzed from more than three experiments); (b) Arrhenius plots and the activation energy (E_a) of PEPL and PEPA electrolytes; (c) Raman spectra of PEPL and PEPA electrolytes; (d) TGA curves of PEPL and PEPA electrolytes

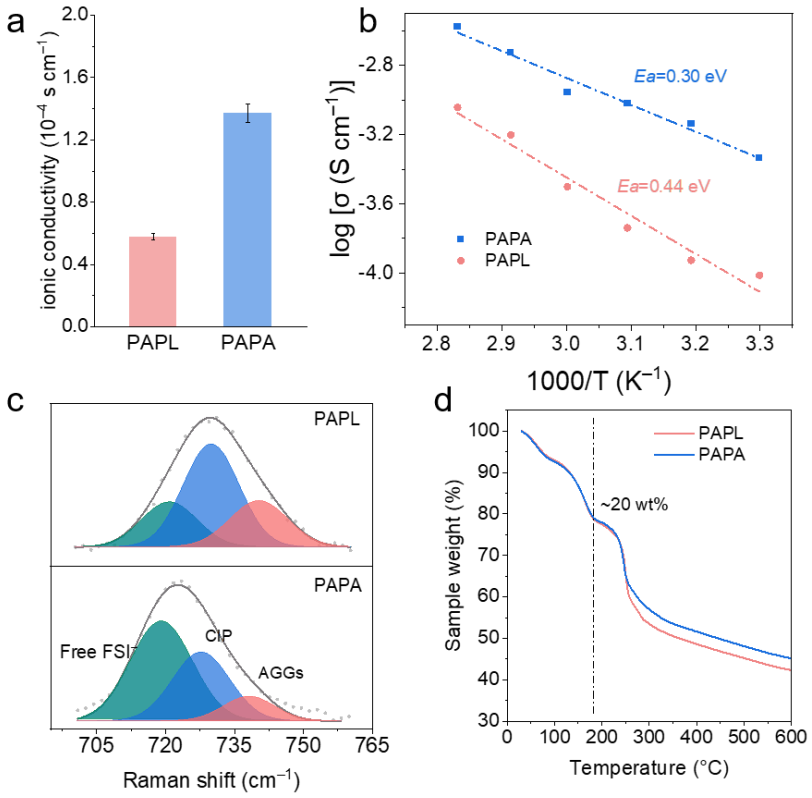

313

314 **Supplementary Fig. 40** (a) The ionic conductivity of PAPL and PAPA electrolytes (Data were
315 analyzed from more than three experiments); (b) Arrhenius plots and the activation energy (E_a) of
316 PAPL and PAPA electrolytes; (c) Raman spectra of PAPL and PAPA electrolytes; (d) TGA curves of
317 PAPL and PAPA electrolytes

318

319

320

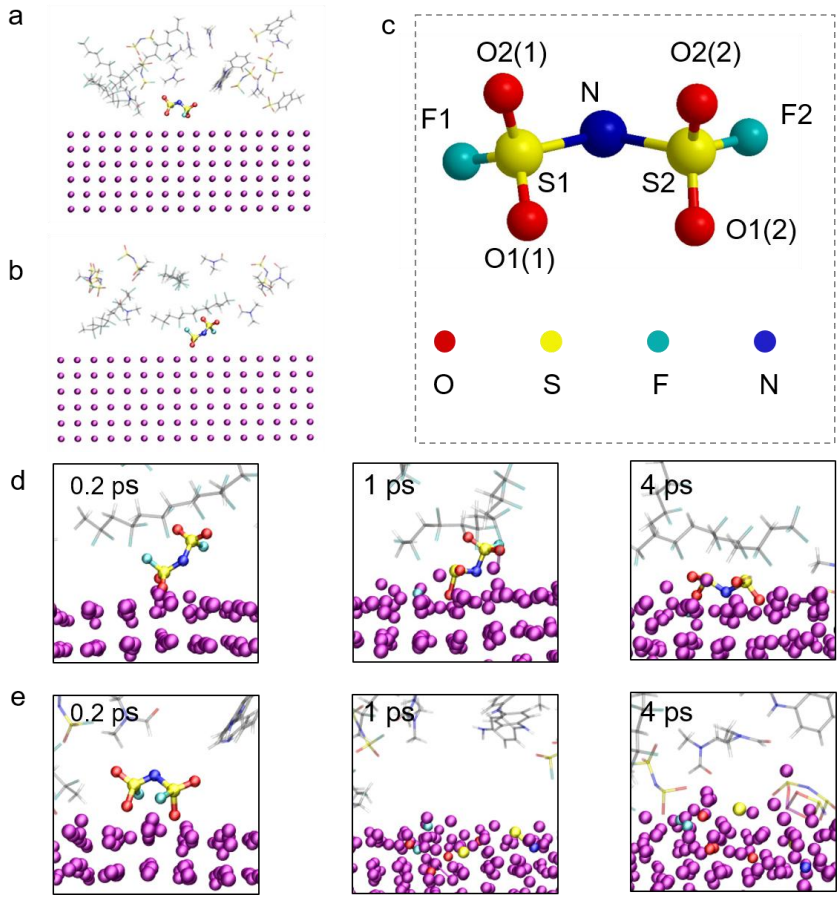

Supplementary Fig. 41 Initial configurations of AIMD in the PLPA electrolyte (a) and the PVPL electrolyte (b); Illustration and atom labelling of the FSI^- molecule (c); The representative snapshots of 0.2, 1 and 4 ps AIMD simulations in the (d) PVPL and (e) PLPA electrolytes.

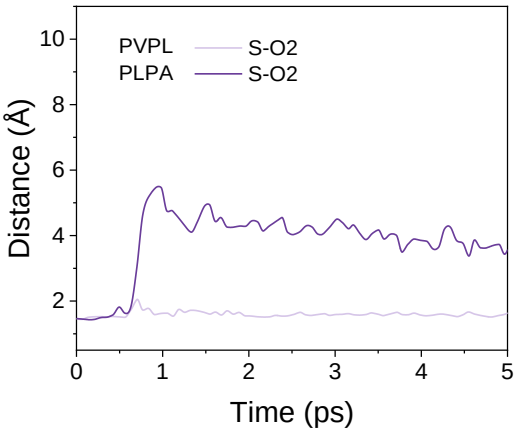

326

327 **Supplementary Fig. 42** Temporal evolution of changes in the bond distance of S–O2 bonds

328

329

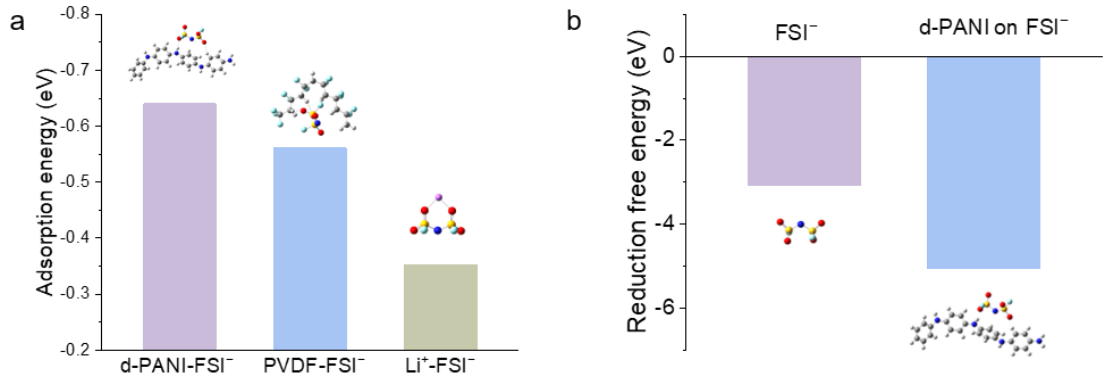

Supplementary Fig. 43 (a) DFT results for adsorption energies; (b) The reduction free energy of FSI^- and d-PANI on FSI^-

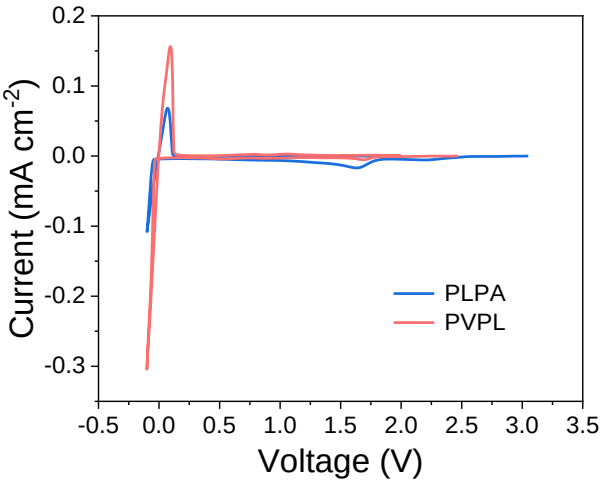

Supplementary Fig. 44 The CV measurements of solid-state Li||Cu cells with different electrolytes

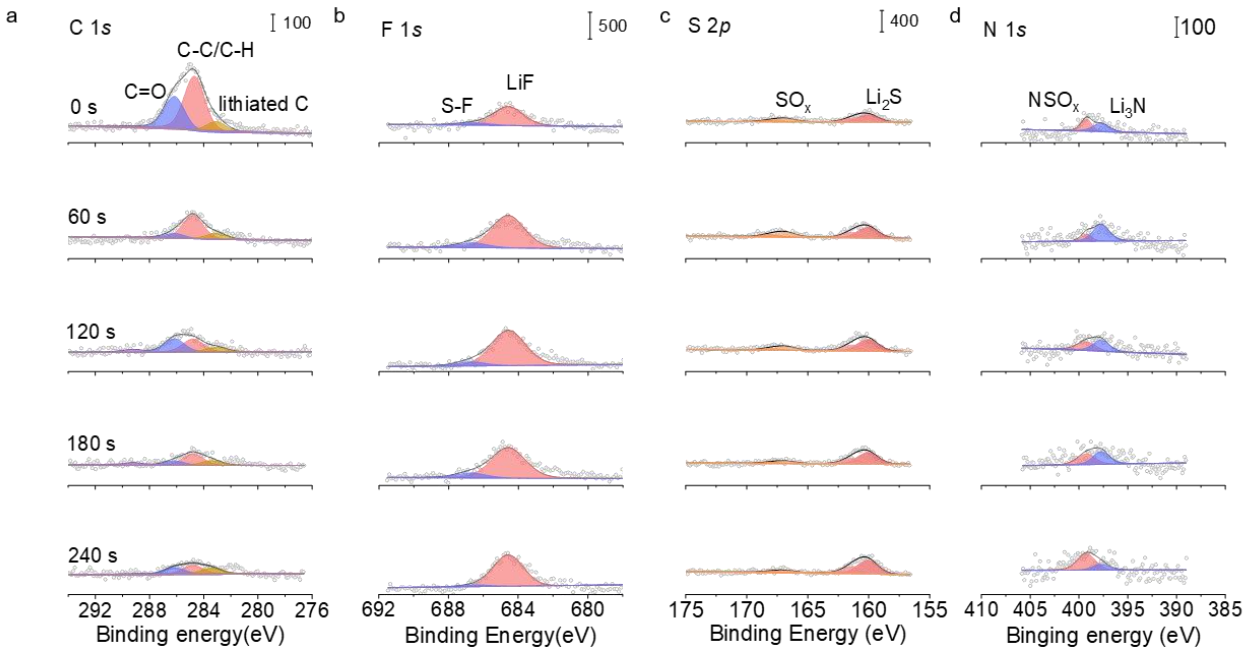

336

337 **Supplementary Fig. 45** XPS depth profiles of C 1*s* (a), F 1*s* (b), S 2*p* (c) and N 1*s* (d) on the cycled

338 Li metal after 50 times Li plating/stripping at 0.1 mA cm^{-2}, 0.1 mAh cm^{-2} (25℃) for the PVPL-driven

339 SEI

340

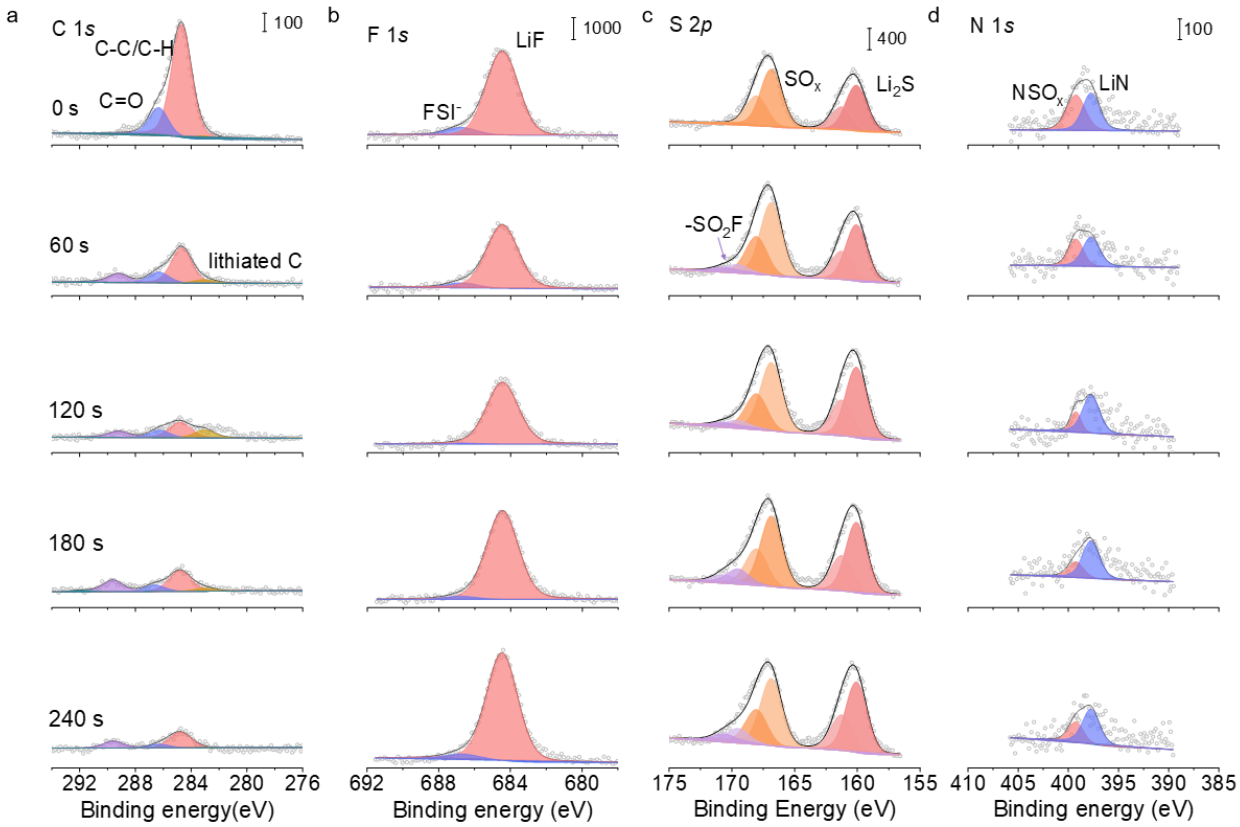

341

342 **Supplementary Fig. 46** XPS depth profiles of C 1*s* (a), F 1*s* (b), S 2*p* (c) and N 1*s* (d) on the cycled

343 Li metal after 50 times Li plating/stripping at 0.1 mA cm^{-2}, 0.1 mAh cm^{-2} (25°C) for the PLPA-driven

344 SEI

345

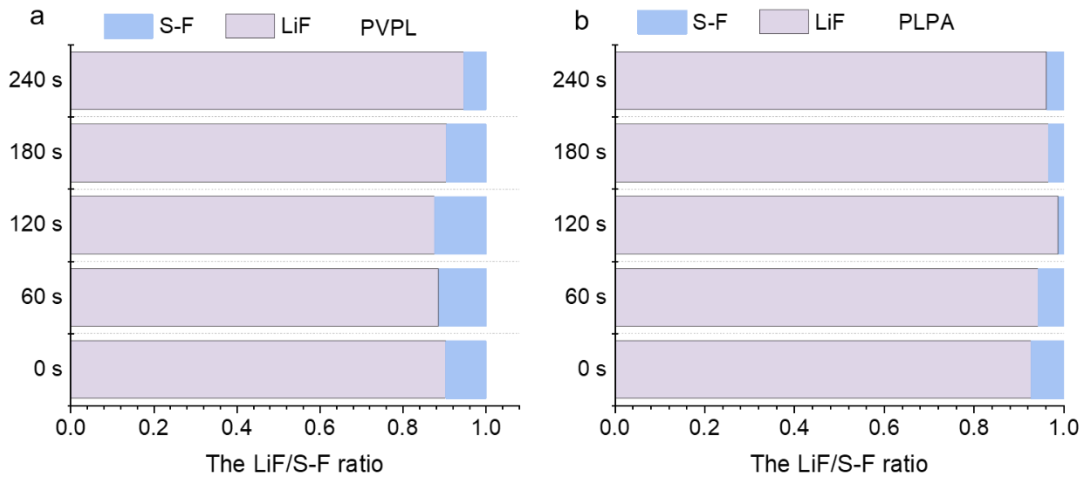

346

347 **Supplementary Fig. 47** The S–F/LiF ratio supported by XPS depth profiling of (a) PVPL electrolyte

348 and (b) PLPA electrolyte

349

350

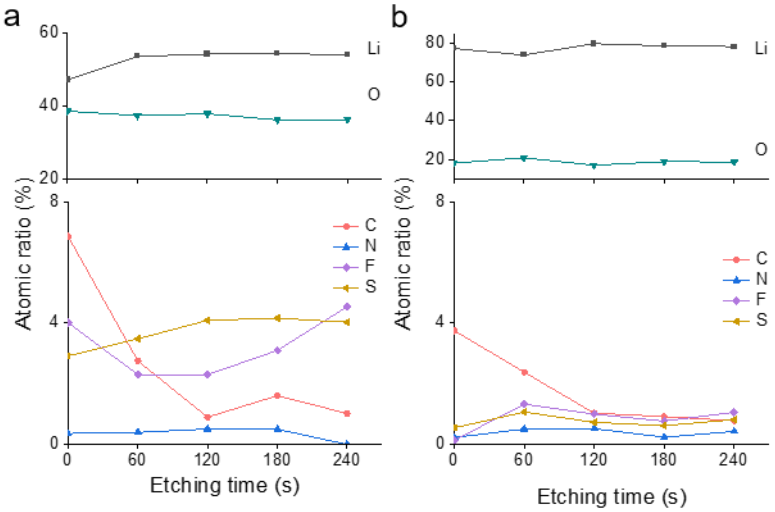

Supplementary Fig. 48 Quantified SEI atomic composition ratios of the (a) PLPA-driven SEI and (b) PVPL-driven SEI

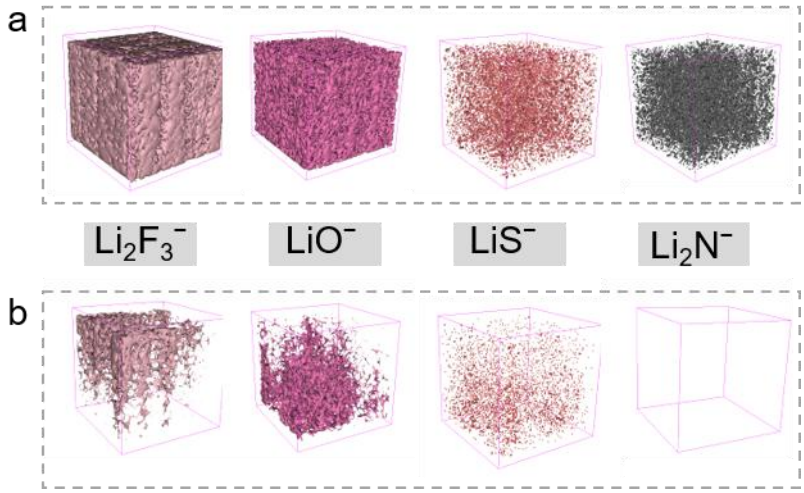

355

356 **Supplementary Fig. 49** The 3D views in the time-of-flight secondary-ion mass spectrometry (ToF-
357 SIMS) sputtered volumes of the PLPA-driven SEI (a) and PVPL-driven SEI (b)
358

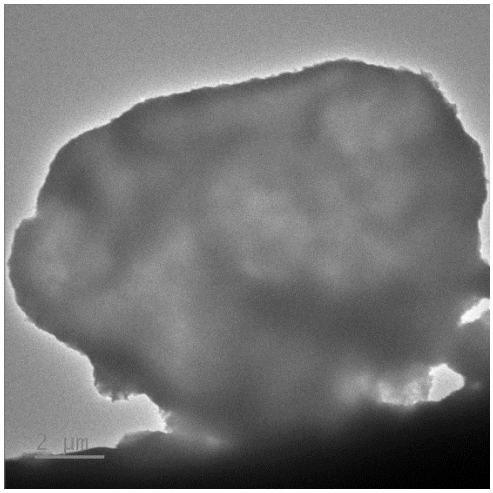

Supplementary Fig. 50 Cryo-TEM image of Li deposition morphology using the PLPA electrolyte

The **supplementary Fig. 50** shows the imaging of the morphology of Li that is deposited using PLPA electrolyte with a current density of 0.1 mA cm^{-2} for 5 hours with a spherical shape morphology.

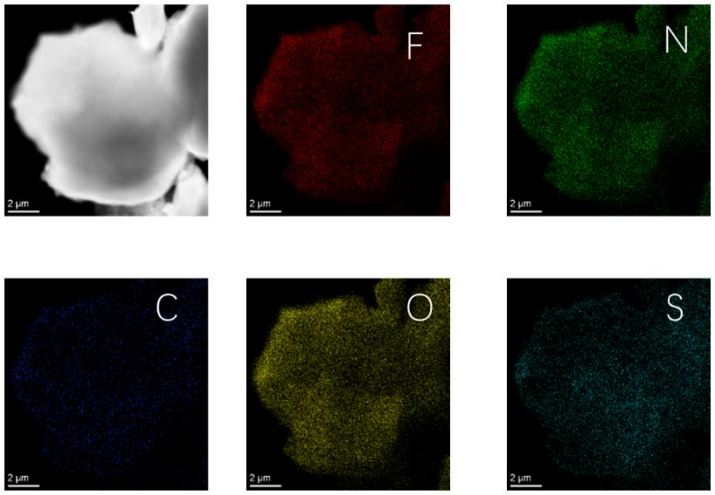

364

365 **Supplementary Fig. 51** Cryo-TEM energy-dispersive X-ray spectroscopy (EDS) maps of the SEI on

366 the Li surface in the PLPA electrolyte

367

368

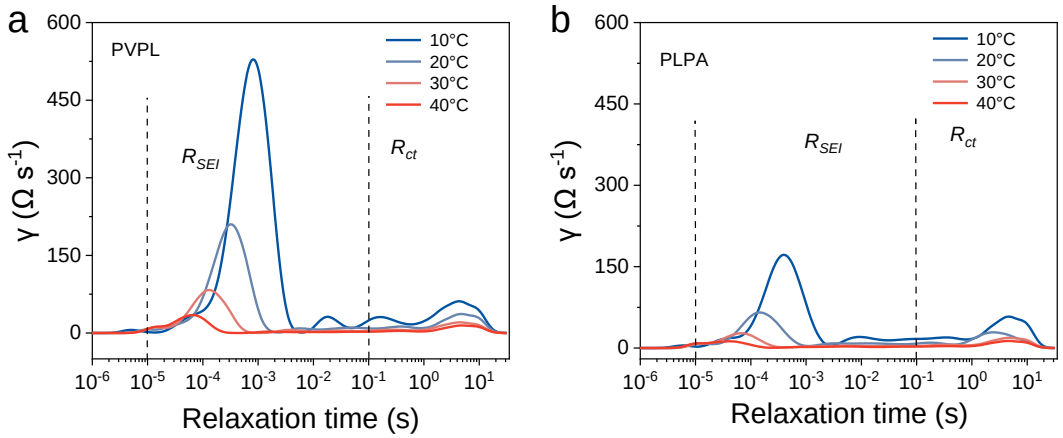

Supplementary Fig. 52 Temperature variable DRT analysis for Li||Li cells with the PVPL electrolyte (a) and PLPA electrolyte (b)

The intermediate frequency peak with the time constants (τ) of 10^{-2} to 10^{-4} corresponds to the impedance of Li^+ diffusion across the SEI (R_{SEI}).

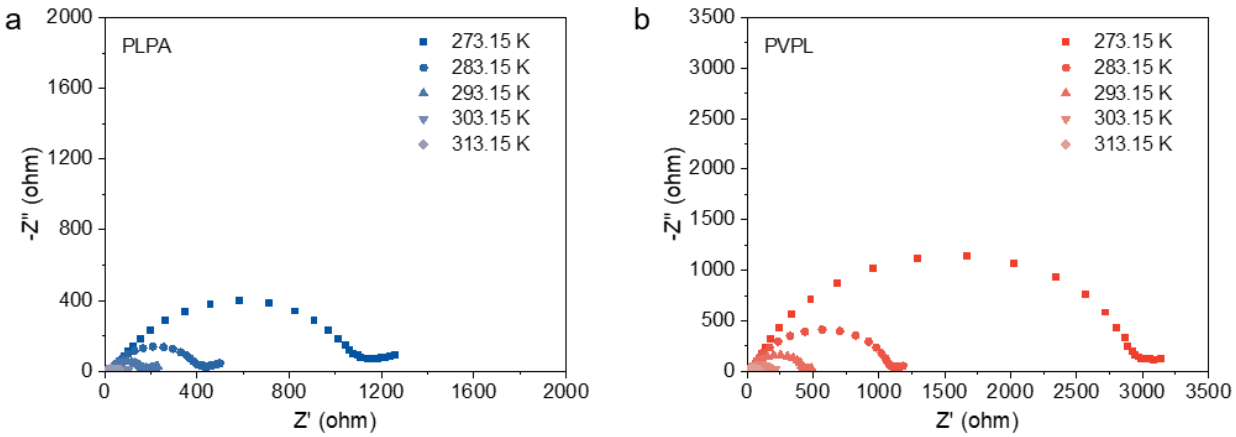

375

376 **Supplementary Fig. 53** Nyquist plots at various temperatures for symmetric Li cells after forming

377 stable SEI with the PLPA electrolyte (a) and PVPL electrolyte (b)

378

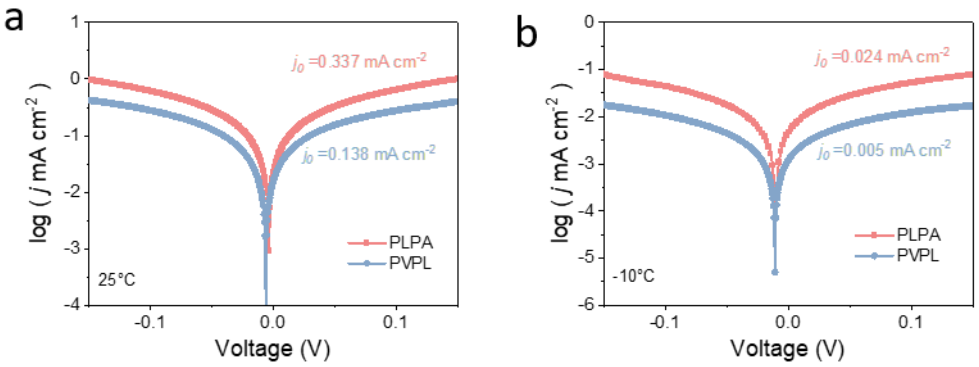

Supplementary Fig. 54 Tafel plots of the Li||Li cells with different electrolytes at 25°C (a) and −10°C (b)

The exchange current density (j_0,) obtained from Tafel plots in the PLPA electrolyte demonstrates a much higher j_0 of 0.337 mA cm^{-2} at 25°C than that using PVPL electrolyte (0.138 mA cm^{-2}). When the temperature drops to −10°C, the PLPA electrolyte still exhibits the higher j_0 than PVPL electrolyte.

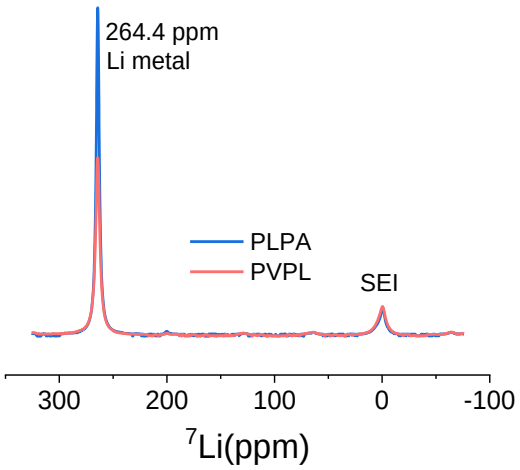

Supplementary Fig. 55 1D ^{7}Li MAS spectra of the Li and SEI generated in the PVPL electrolyte and PLPA electrolyte

To discriminate between the different Li-containing species present in SEI and metallic Li after directly plating Li on a Cu substrate with different SPEs at 0.1 mA cm^{-2}, one-pulse ^{7}Li magic angle spinning (MAS) solid-state nuclear magnetic resonance (ss-NMR) spectra were measured. Two distinguishable resonances were observed in the spectrum, which correspond to the two main kinds of Li environment. One is from metallic Li and the other from Li species in the generated SEI.

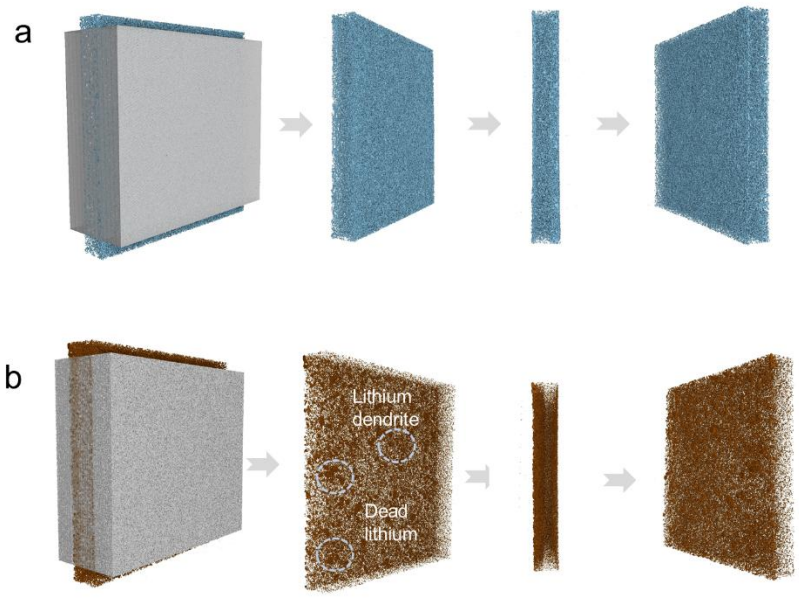

Supplementary Fig. 56 Cross-sectional synchrotron X-ray tomography images showing of (a) Li|PLPA|Li cells and (b) Li|PVPL|Li cells after cycling

Supplementary Note 5| The morphology of cycled Li negative electrodes

The X-ray computed tomography (CT) scans display the original non-destructive information of the morphology and internal structure of the cell. Therefore, the dendrite growth in the symmetric cells was investigated by the X-ray CT. The Li|PLPA|Li cell and Li|PVPL|Li cell were plated/ stripped for 100 cycles at a current density of 0.5 mA cm^{-2} and a capacity of 0.5 mAh cm^{-2} for ex situ X-ray CT scans. As shown in **Supplementary Fig. 56a,** there were no obvious Li dendrites and dead Li coverage on the surface of the PLPA electrolyte. In contrast, the dendrite growth is observed in the PVPL electrolyte and uneven Li deposits trigger severe dead Li to coverage on the surface of the PVPL electrolyte (**Supplementary Fig. 56b**).

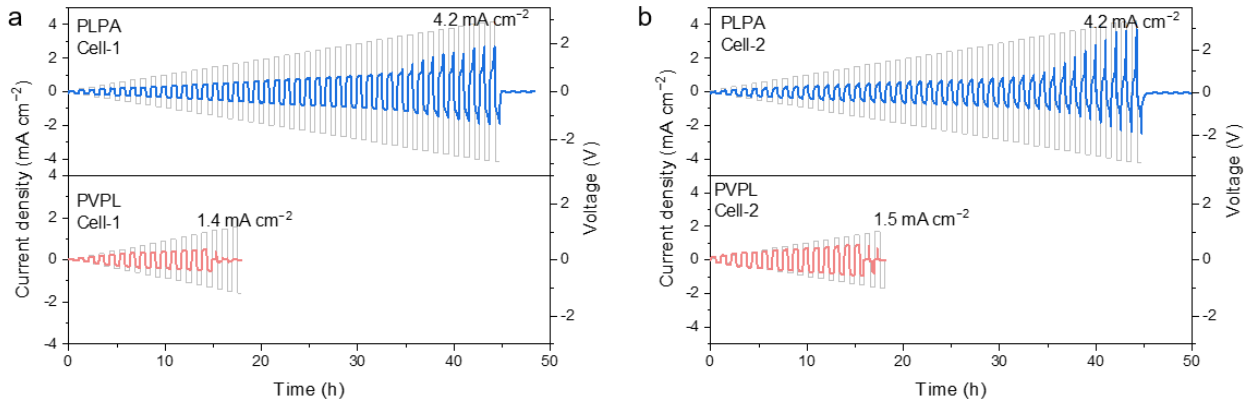

409

410 **Supplementary Fig. 57** (a) Critical current density measurement of the Li||Li cell-1 using PVPL
411 electrolyte and PLPA electrolyte at 25°C and 0.1 mA cm^{-2} increased per step; (b) Critical current
412 density measurement of the Li||Li cell-2 using PVPL electrolyte and PLPA electrolyte at 25°C and
413 0.1 mA cm^{-2} increased per step

414

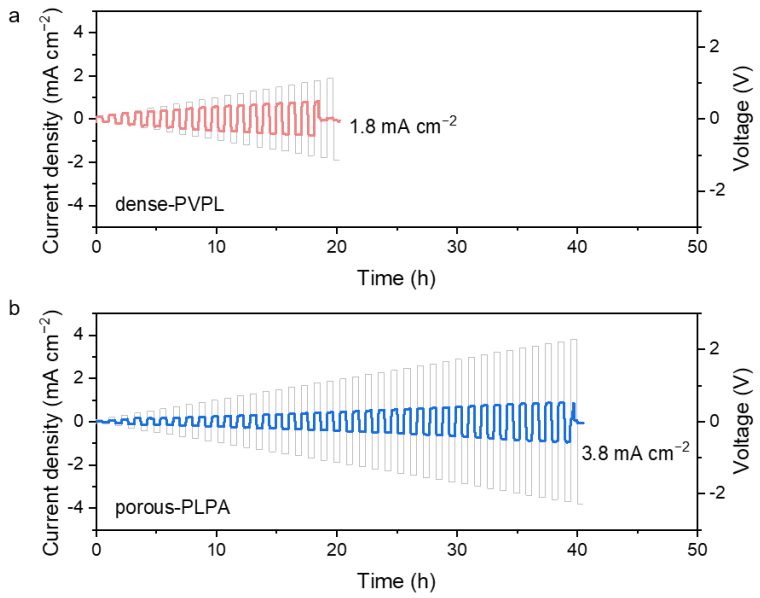

415

416 **Supplementary Fig. 58** Critical current density measurement of the Li||Li cells using (a) the dense-

417 PVPL electrolyte and (b) the porous-PLPA electrolyte at 25°C and 0.1 mA cm^{-2} increased per step

418

419

Supplementary Note 6| The influence of electrolyte microstructure on interface stability

The critical current density (CCD) tests of the Li|porous-PLPA|Li cells and Li|dense-PVPL|Li were performed to evaluate the ability to inhibit the growth of Li dendrites. The dense-PVPL electrolyte exhibits a CCD of 1.8 mA cm^{-2} (**Supplementary Fig. 58a**), which is slightly higher than that of the PVPL electrolyte (1.4 mA cm^{-2}), but significantly lower than that of the PLPA electrolyte (4.2 mA cm^{-2}). The porous-PLPA electrolyte exhibits a CCD of 3.8 mA cm^{-2} (**Supplementary Fig. 58b**), which is significantly higher than that of the PVPL electrolyte (1.4 mA cm^{-2}) and dense-PVPL electrolyte (1.8 mA cm^{-2}). The results indicate that a dense structure of polymer electrolyte provides only partial physical blocking to Li propagation, while not achieving a homogeneous Li deposition that demands a robust solid electrolyte interphase (SEI) with fast transport kinetics to enable interfacial stability against Li metal, demonstrating the vital role of the electron delocalization-driven SEI with the inorganic components in suppressing the growth of Li dendrites and enabling stable interface.

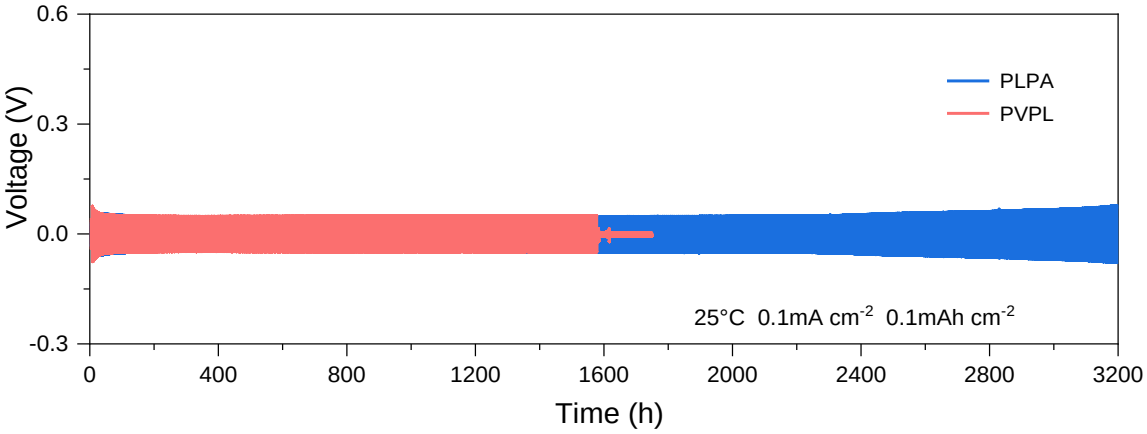

434

435 **Supplementary Fig. 59** Galvanostatic Li plating/stripping curves of the Li||Li cells using the PVPL

436 electrolyte and PLPA electrolyte at 0.1 mA cm^{-2}, 0.1 mAh cm^{-2} at 25°C

437

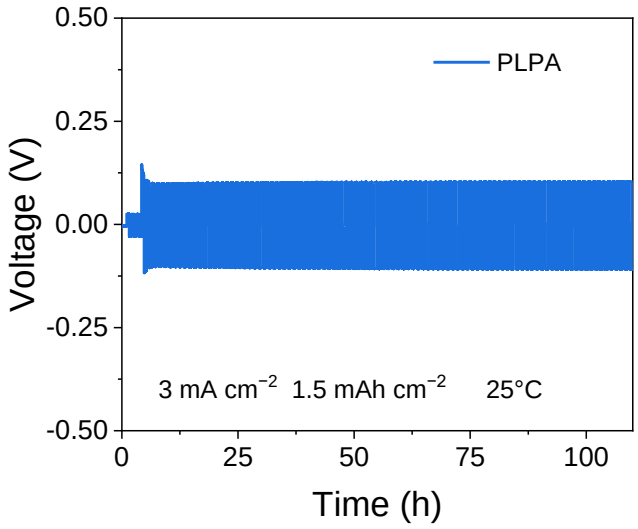

Supplementary Fig. 60 Galvanostatic Li plating/stripping curves of the Li||Li cells using the PLPA electrolyte at 3 mA cm^{-2}, 1.5 mAh cm^{-2} at 25°C

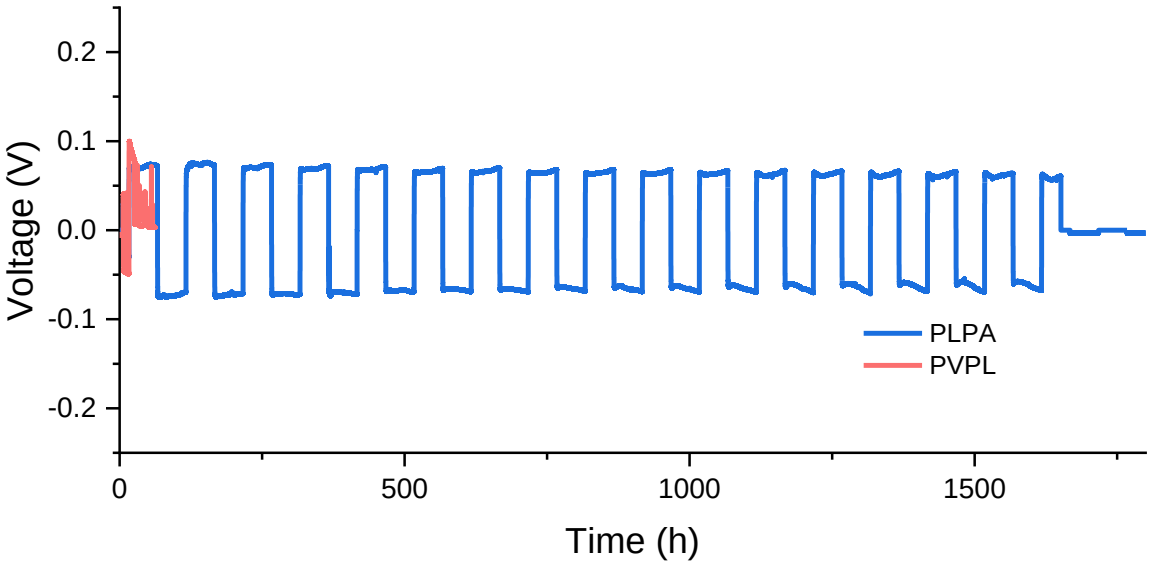

Supplementary Fig. 61 Galvanostatic Li plating/stripping curves of the Li||Li cells using the PVPL and PLPA electrolyte at 0.1 mA cm^{-2} and 5 mAh cm^{-2} at 25°C

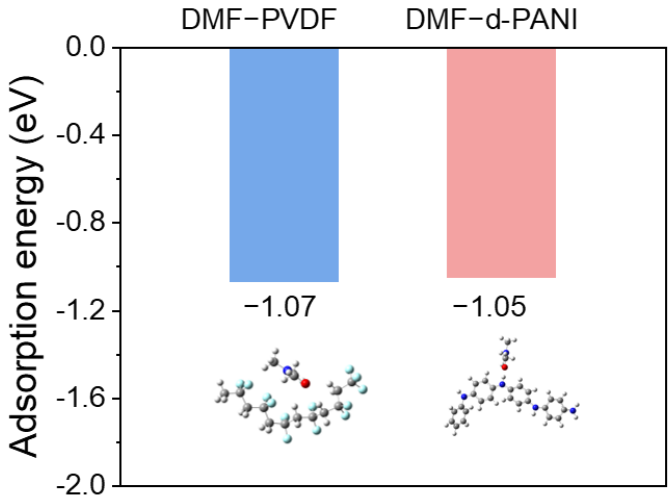

446

447 **Supplementary Fig. 62** DFT results for adsorption energies between PVDF, d-PANI and DMF

448

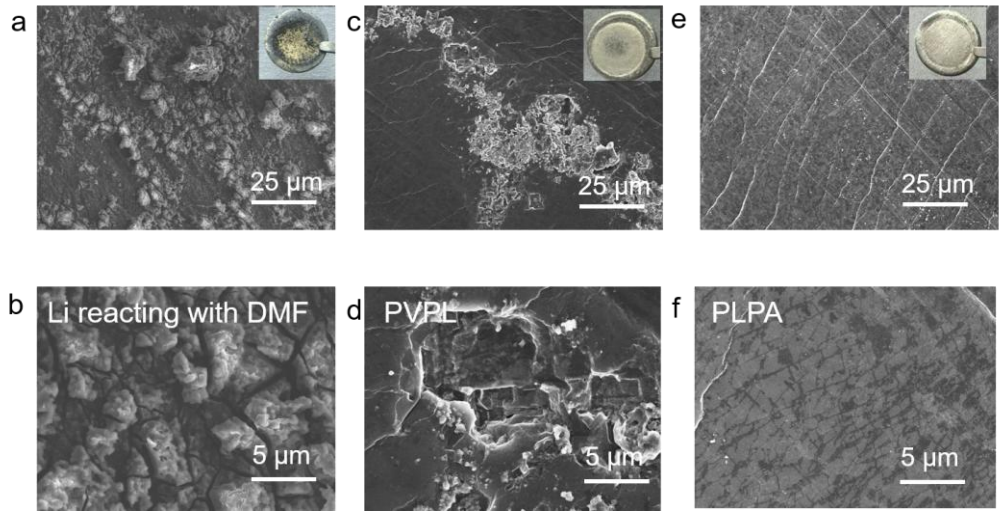

449

450 **Supplementary Fig. 63** The SEM image of Li negative electrode after direct contact with DMF (a,

451 b), cycled with PVPL electrolyte (c, d) and cycled with PLPA electrolyte (e, f)

452

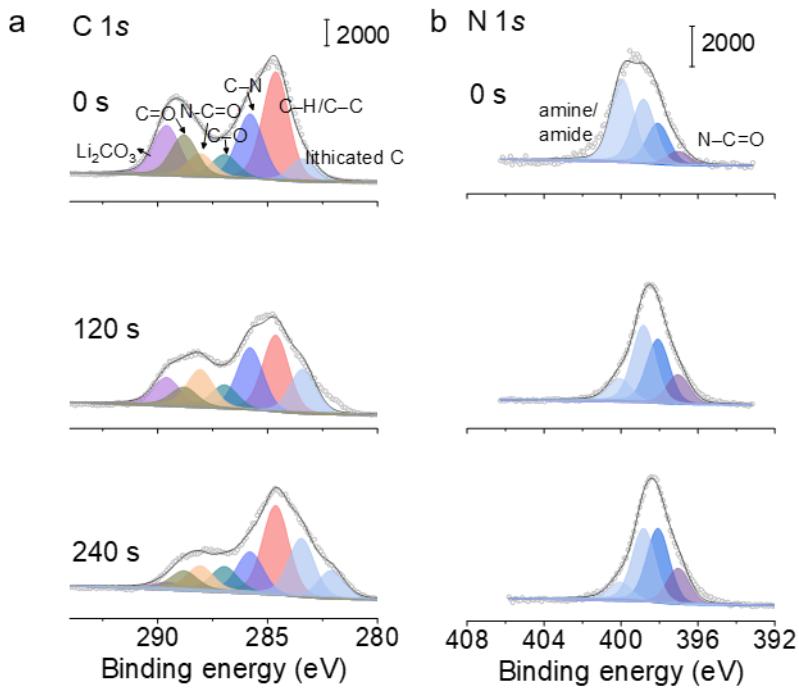

453

454 **Supplementary Fig. 64** XPS depth profiles of C 1*s* (a), N 1*s* (b) on the Li foil after the reaction with

455 pure DMF solvent

456

457

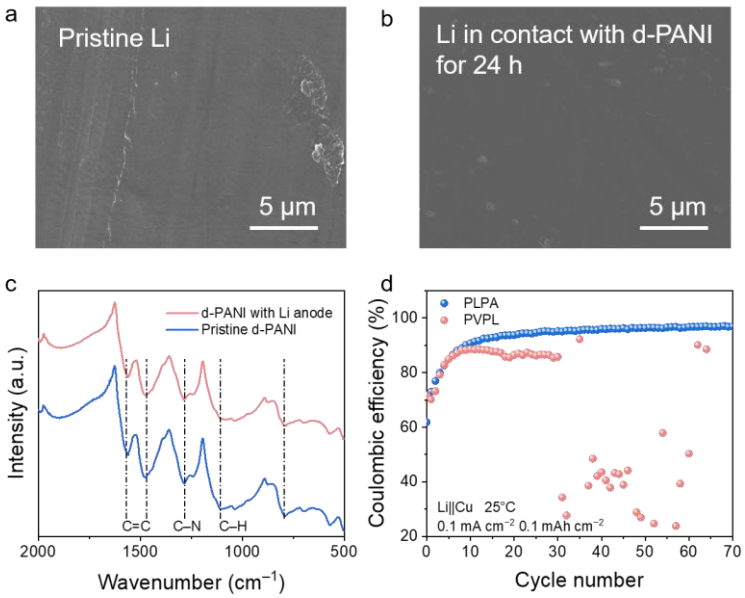

458

459 **Supplementary Fig. 65** The SEM images of (a) pristine Li and (b) Li contact with d-PANI for 24h;
460 (c) FTIR spectra of pristine d-PANI and d-PANI with Li negative electrode; (d) the coulombic
461 efficiency of Li||Cu cells with PVPL and PLPA electrolytes under full plating/stripping conditions at
462 0.1 mA cm^{-2} and 0.1 mAh cm^{-2}

463

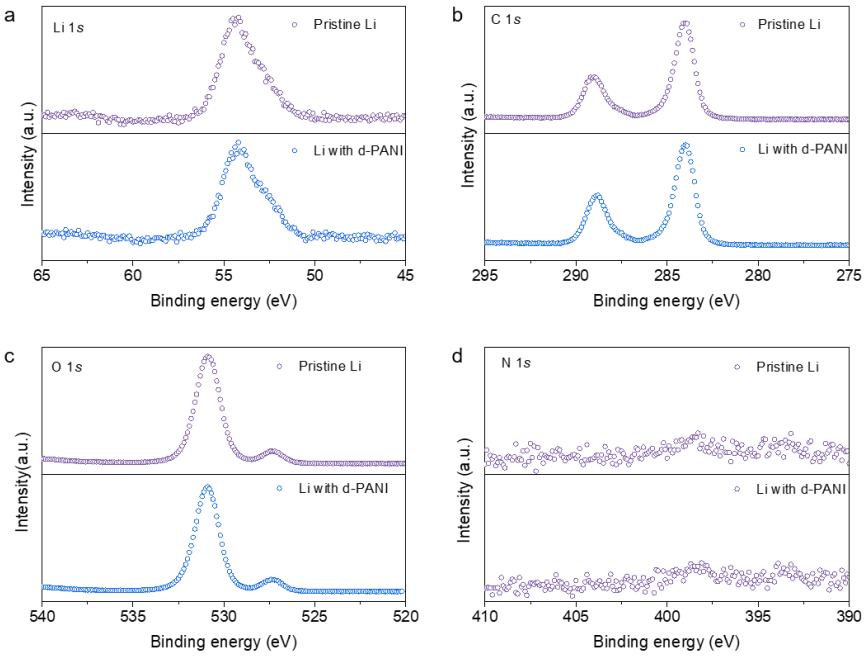

464

465 **Supplementary Fig. 66** XPS depth profiles of Li 1*s* (a), C 1*s* (b), O 1*s* (c) and N 1*s* (d) on the pristine

466 Li foil and the Li foil after direct contact with d-PANI

467

468

Supplementary Note 7| Influence of d-PANI and DMF for side reactions with Li

Density functional theory (DFT) calculations were performed to investigate the interaction between the PVDF, DMF and d-PANI (**Supplementary Fig. 62**). The adsorption energy of the DMF with PVDF and d-PANI is −1.07 eV and −1.05 eV, respectively, indicating that d-PANI does not exhibit strong interaction with DMF to effectively suppress their decomposition. Furthermore, the surface morphologies of the Li negative electrode in the Li||Li cell after cycling 100 h were also monitored. As shown in **Supplementary Fig. 63**, the surface of Li metal after direct contact with DMF exhibits severe side reactions, leading to surface cracking and the formation of side reaction products. In contrast, the Li metal surfaces after cycling with PVPL and PLPA electrolytes all are no morphology of serious side reactions. For the PVPL electrolyte, some irregular Li deposition and stripping patterns are observed on the Li metal surface. The surface of Li metal with PLPA electrolyte remains smooth due to the homogeneous Li deposition and stripping induced by a robust anion-derived SEI. To further investigate the interfacial side reactions between the composite solid-state electrolyte and Li metal, the depth-profiling X-ray photoelectron spectroscopy (XPS) measurement of Li metal was performed. When DMF is directly absorbed on a Li foil, C–N, N–C=O and amine/amide peaks are detected on the surface of the Li foil after the reaction with DMF solution, suggesting the reaction between DMF and Li metal (**Supplementary Fig. 64**). However, these peaks are not detected on the Li metal surface after cycling with the composite solid-state electrolyte, indicating that the side reactions between DMF and Li metal were significantly suppressed (**Supplementary Fig. 45, 46**).

Furthermore, to investigate the stability between d-PANI and Li metal, d-PANI was coated onto a Li foil surface for 24 hours and subsequently removed. The scanning electron microscope (SEM) images of the contacted Li surface retain a smooth morphology, which is identical to that of a fresh Li foil (**Supplementary Fig. 65a, b**). Furthermore, the FTIR spectra showed no significant change in d-PANI before and after the contact with Li foil. These results demonstrate that no serious side reactions occur between d-PANI and Li metal (**Supplementary Fig. 65c**). Meanwhile, no significant changes were observed in the XPS peaks on the surface of the pristine Li foil and the Li foil after direct contact with d-PANI (**Supplementary Fig. 66**), indicating that no severe side reactions occur between d-PANI and Li metal.

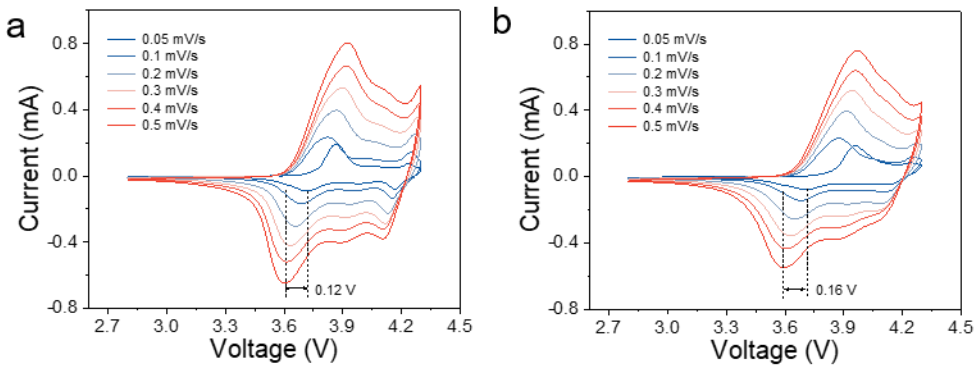

Supplementary Fig. 67 CV measurements of the (a) Li|PLPA|NCM811 and (b) Li|PVPL|NCM811 cells at different scan rates

The CV curves at different scanning rate indicate that the Li|PLPA|NCM811 cell possesses much superior reversibility of redox reaction of and the smaller overpotential than the Li|PVPL|NCM811 cell.

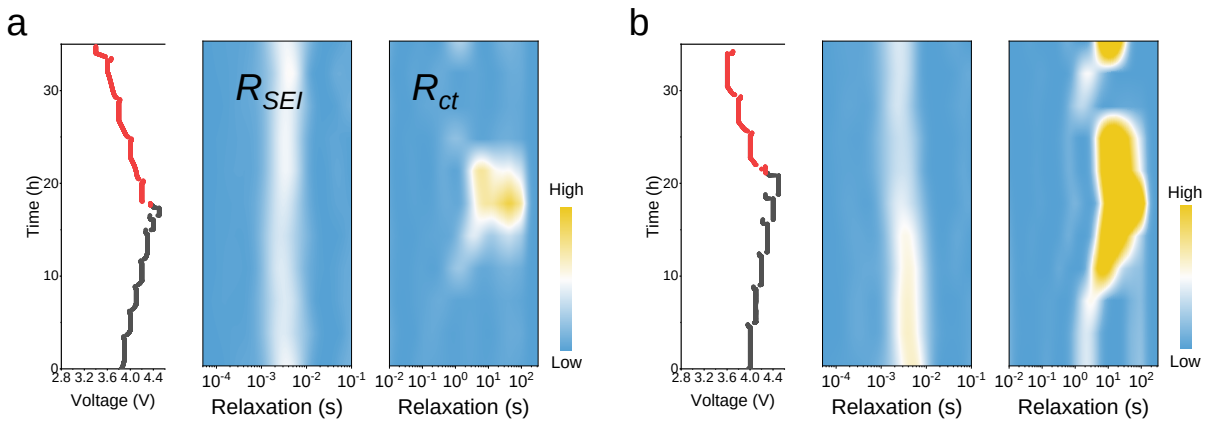

505

506 **Supplementary Fig. 68** In situ DRT data representing different SOCs of the Li||NCM811 cells with
507 the PLPA electrolyte (a) and PVPL electrolyte (b) at −10°C

508 Compared to the Li||NCM811 cells with the PVPL electrolyte, the negligible R_{ct} and R_{SEI} in the PLPA
509 electrolyte at different state of charge are observed in **Supplementary Fig. 68** of in situ EIS-combined
510 DRT mapping.

511

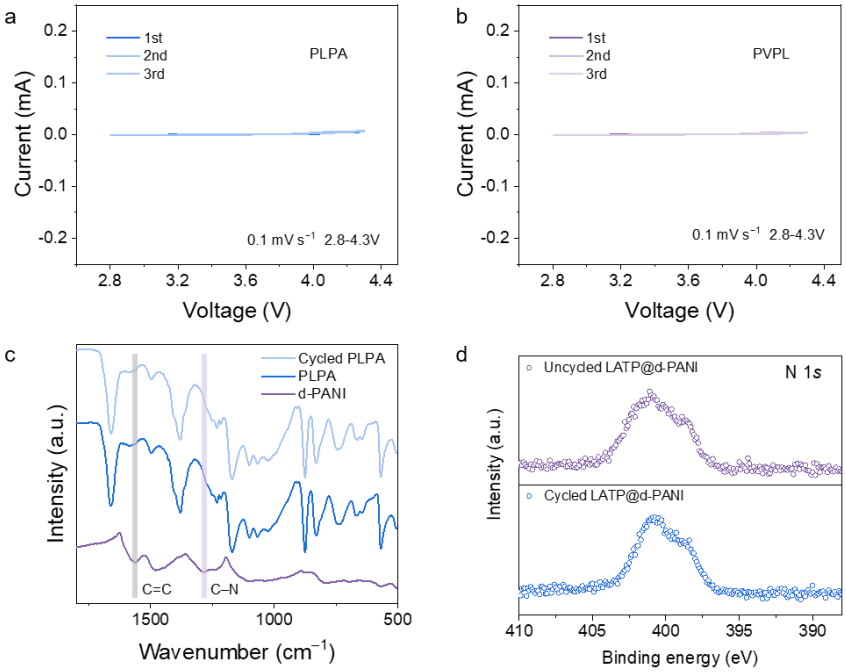

Supplementary Fig. 69. The CV measurements of Li||SS cells with (a) the PLPA and (b) PVPL electrolyte; (c) The FTIR spectroscopy of d-PANI, PLPA and cycled PLPA electrolyte; (d) The XPS of uncycled and cycled LATP@d-PANI

To investigate the evolution of d-PANI during battery operation, the Li||stainless steel (SS) cells with PVPL and PLPA electrolytes were assembled to perform cyclic voltammetry (CV) measurements in the voltage range of 2.8–4.3 V for 3 cycles. As shown in **Supplementary Fig. 69a, b**, no other peaks appeared in the CV curves of Li||SS cells with PLPA electrolyte compared to that with PVPL electrolyte, indicating that no additional reactions of d-PANI occurred for PLPA electrolyte during cell's cycling process. In addition, Fourier-transform infrared (FT-IR) spectroscopy and X-ray photoelectron spectroscopy reveal that the characteristic signals of d-PANI in the PLPA electrolyte show no significant change before and after cycling (**Supplementary Fig. 69c, d**). These results demonstrate that the d-PANI remains stable during cell's cycling process, which can be attributed to the uniform dispersion of d-PANI particles throughout the solid polymer electrolyte.

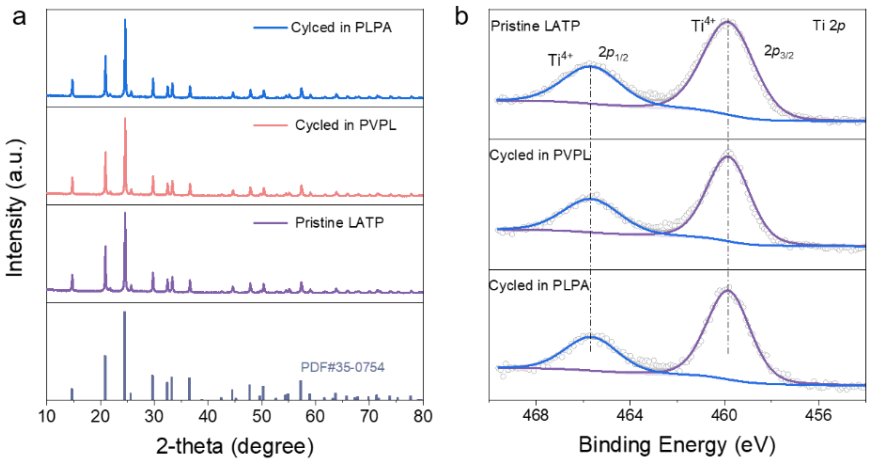

526

527 **Supplementary Fig. 70** (a) The XRD patterns (b) XPS spectra for Ti 2*p* of pristine LATP and LATP

528 from cycled in PVPL electrolyte and PLPA electrolyte

529

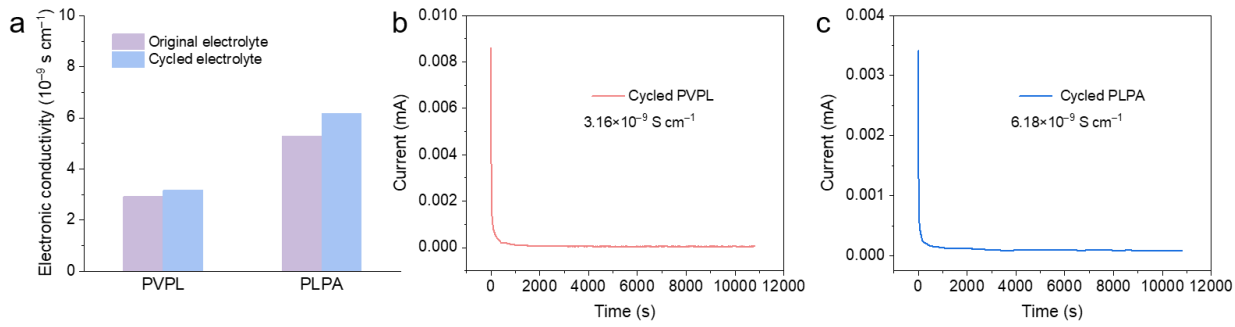

530

531 **Supplementary Fig. 71** (a) The electronic conductivity of original and cycled electrolytes; Current-

532 time curves of symmetric cells with stainless-steel electrodes for the electronic conductivity of cycled

533 (b) PVPL electrolyte and (c) PLPA electrolyte

534

535

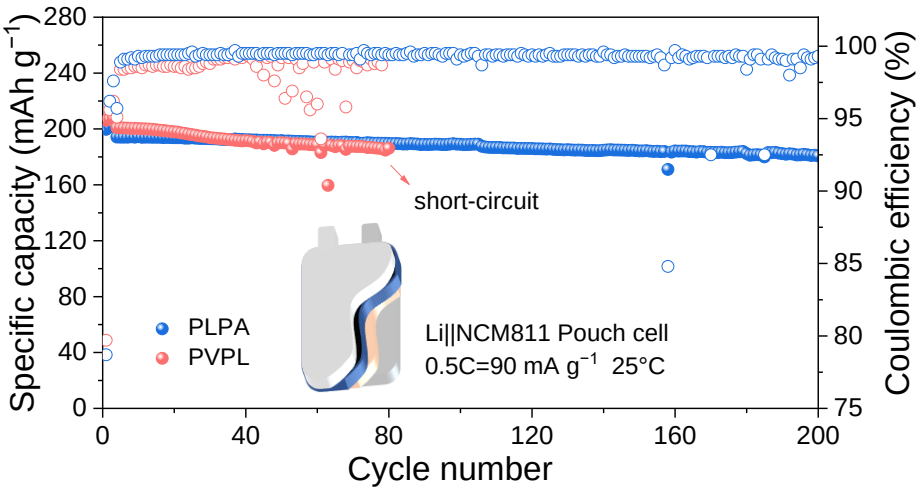

536 **Supplementary Fig. 72** Cycling performance of Li||NCM811 pouch cells using different electrolytes

537 at 90 mA g^{-1} and 25°C

538

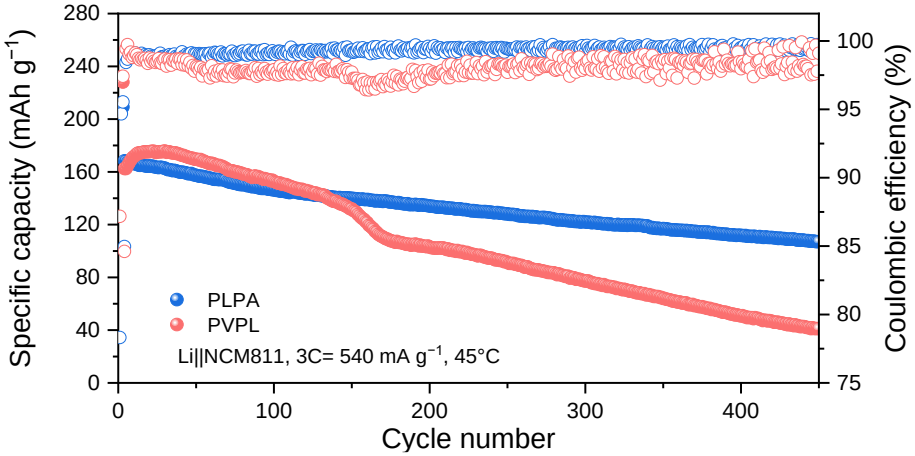

539

540 **Supplementary Fig. 73** Cycling performance of the Li||NCM811 cells using different electrolytes at
541 540 mA g^{-1} and 45°C

542 The Li|PVPL|NCM811 cells show serious fluctuation of Coulombic efficiency, followed by a rapid
543 capacity decay due to the uncontrollable side reactions between the PVPL electrolyte and Li negative
544 electrode at an elevated temperature of 45°C.

545

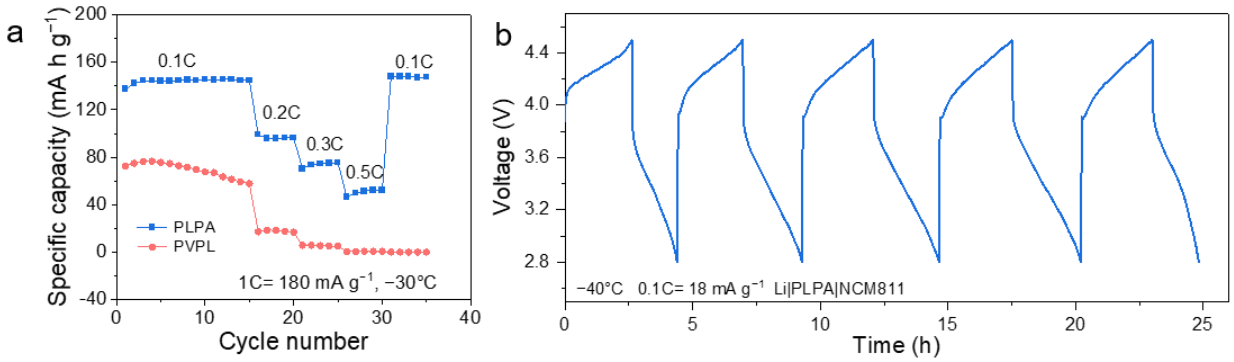

546

547 **Supplementary Fig. 74** (a) Rate capacities of Li||NCM811 cells with different electrolytes at –30°C;

548 (b) Charge-discharge curves of Li||NCM811 cells with PLPA electrolytes at –40°C

549

Supplementary Table

Supplementary Table 1. The reduction potential of Li-anion complex and the diffusion coefficients of Li^+ ions at varying molar ratios of ligand and Li salt

Molar ratios of ligand and Li salt	**Li^+ diffusion coefficient ($cm^2\ s^{-1}$)**	**The onset of the reduction potential of Li-anion complex**
1:1	9.677×10^{-11}	–0.765
1.4:1	3.166×10^{-10}	–0.875
1.6:1	9.077×10^{-10}	–0.930
2:1	3.085×10^{-9}	–1.039
3:1	5.150×10^{-9}	–1.229

555 **Supplementary Table 2**. Comparison of electronic conductivities of the PLPA electrolyte with
556 other reported electrolyte systems

Ref. number	Electrolyte System	Electronic conductivity (10^{-9} S cm^{-1})	Reference
1	LLZO/Li_3AlF_6	12.70	*Adv. Mater. 35, 2208951 (2023)*[5]
2	Li_3YCl_6	2.80	*Adv. Mater. 30, 1803075 (2018)*[6]
3	LiF-$Li_{10}GeP_2S_{12}$	2.42	*Adv. Mater. 35, 2211047 (2023)*[7]
4	Li_3PS_4	5.00	*Energy Environ. Sci. 11, 2828-2832 (2018)*[8]
5	LLZTO-SnO_2-PTAA	1.02	*Adv. Mater. e15687 (2025)*[9]
6	$Li_{5.5}PS_{4.5}Cl_{0.75}Br_{0.75}$	9.70	*Angew. Chem. Int. Ed. 65, e23225 (2026)*[10]
7	$Li_3Ta_3O_4Cl_{10}$	7.79	*Science 390, 199-204 (2025)*[11]
8	PVDF/Ag-LLZTO	3.54	*Nature 647, 86-92 (2025)*[12]
9	PEO/LiTFSI/carbon	6.83	*Angew. Chem. Int. Ed. 62, e202217538 (2023)*[13]
10	**PVDF/ d-PANI**	**5.27**	***This work***

557

558

559 **Supplementary Table** 3 Comparative data of conductivity enhancement of our work with other
560 high-dielectric materials

Ref. number	Electrolyte System	Ionic conductivity (10^{-4} S cm^{-1})	Reference
1	$BaTiO_3$–$Li_{0.33}La_{0.56}TiO_{3-x}$/ PVDF	8.20	*Nat. Nanotechnol 18, 602-610 (2023)*[14]
2	$BaTiO_{3-x}$/PVDF	8.40	*Energy Environ. Sci. 17, 3797-3806 (2024)*[15]
3	$LiNbO_3$/PVDF	7.39	*Sci. China Mater. 67, 1947–1955 (2024)*[16]
4	Si_3N_4/PVDF	5.70	*Energy Storage Mater. 53, 305-314 (2022)*[17]
5	CuPcLi/PVT	8.30	*Adv. Energy Mater. 13, 2204425 (2023)*[18]
6	$Ca_2Nb_3O_{10}$/PEO	2.40	*Energy Storage Mater. 70, 103473 (2024)*[19]
7	$PbZr_xTi_{1-x}O_3$/PVDF	1.16	*ACS Nano 17, 14114–14122 (2023)*[20]
8	$LiTaO_3$/PVDF	4.90	*Energy Mater. Devices 1, 9370004 (2023)*[21]
9	$Li_{0.3}Ti_{0.02}Ni_{0.68}O$/PVDF	4.09	*Carbon Neutrality 3, 22 (2024)*[22]
10	**PLPA**	**8.92**	***This work***

561

Supplementary Table 4 Comparative data of Li||Li cells cycling performance of our work and previously published studies

Ref. number	**Electrolyte**	**Current density (mA cm^{-2})**	**Areal capacity (mAh cm^{-2})**	**Cycle time (hours)**	**Ref.**
1	**PLPA**	**2.0**	**1.0**	**1, 200**	**This work**
2	**PLPA**	**0.1**	**0.1**	**3, 200**	**This work**
3	**PLPA**	**0.1**	**5.0**	**1, 500**	**This work**
4	PVDF/LATP	0.5	0.5	700	Ref.[1]
5	PVDF/zeolite	0.5	0.5	200	Ref.[23]
6	PVDF/$NaNbO_3$	1.0	0.5	275	Ref.[24]
7	PVDF/$MoSe_2$	1.0	1.0	480	Ref.[25]
8	PVDF/MOFs	0.5	0.5	500	Ref.[26]
9	PVDF-HFP/TiN	0.2	0.2	320	Ref.[27]
10	PVDF-HFP/PTFEP	0.5	0.5	1000	Ref.[28]
11	PEO/LiDF	0.3	0.3	700	Ref.[29]
12	PolyEA/SN	0.2	1.0	1, 800	Ref.[30]
13	PVDF/BTO-LLTO	1.0	1.0	300	Ref.[14]
14	P(AT-MBA-6F)	0.2	0.2	500	Ref.[31]
15	PVC/LSC/Zn-PI	0.4	0.2	240	Ref.[32]
16	PVDF/FEC	0.1	0.1	1200	Ref.[33]
17	PVDF/FEC	1	1	400	Ref.[33]

Supplementary Table 5 Comparative data of solid-state Li metal batteries cycling performance of our work and previously published studies

Ref. number	Positive electrode	Negative electrode	Electrolyte	Rate	Cycle numbers	Ref.
1	**NCM811**	**Li**	**PLPA**	**5C**	**4,000**	**This work**
2	**NCM811**	**Li**	**PLPA**	**10C**	**13,000**	**This work**
3	NCM811	Li	PVDF/LATP	2C	1,500	Ref.[1]
4	NCM811	Li	PVDF/zeolite	1C	1,130	Ref.[23]
5	NCM811	Li	PVDF/$NaNbO_3$	2C	2,200	Ref.[24]
6	NCM811	Li	PVDF/$MoSe_2$	3C	2,000	Ref.[25]
7	NCM811	Li	PVDF/MOFs	5C	1,000	Ref.[26]
8	$LiFePO_4$	Li	PVDF-HFP/TiN	2C	3,000	Ref.[27]
9	SPAN	Li	PTMG-HDI-BHDS	0.3C	700	Ref.[34]
10	NCM811	Li	PVDF-HFP/PTFEP	0.5C	480	Ref.[28]
11	SPAN	Li	PVDF/$Ni[CN]_4$	1C	1,000	Ref.[35]
12	$LiFePO_4$	Li	PEO/LiDF	0.5C	1,000	Ref.[29]
13	$LiFePO_4$	Li	PolyEA/SN	1C	2,000	Ref.[30]
14	NCM811	Li	PVDF/BTO-LLTO	1C	1,500	Ref.[14]
15	NCM811	Li	P(AT-MBA-6F)	0.2C	1,500	Ref.[31]
16	$LiFePO_4$	Li	PVC/LSC/Zn-PI	1C	800	Ref.[32]
17	$LiFePO_4$	Li	PEO/Li-HA-F	0.2C	500	Ref.[36]
18	SPAN	Li	PVDF-HFP/ SCPBA	0.5C	180	Ref.[37]

NCM811, 1C=180 mA g^{-1}; LFP, 1C=145 mA g^{-1}; SPAN, 1C=811 mA g^{-1}

568 **Supplementary Table 6** The detailed simulation system compositions

	PVPL without electric field	PVPL with electric field	PLPA without electric field	PLPA with electric field
Li^+	200	200	200	200
FSI^-	200	200	200	200
DMF	280	280	280	280
PVDF	146	146	146	146
d-PANI	0	0	10	10

569

Supplementary References

1 Yang, K. *et al.* Stable Interface Chemistry and Multiple Ion Transport of Composite Electrolyte Contribute to Ultra-long Cycling Solid-State $LiNi_{0.8}Co_{0.1}Mn_{0.1}O_2$/Lithium Metal Batteries. *Angew. Chem.-Int. Edit.* **60**, 24668-24675 (2021).

2 Yang, K. *et al.* Weak-Interaction Environment in a Composite Electrolyte Enabling Ultralong-Cycling High-Voltage Solid-State Lithium Batteries. *J. Am. Chem. Soc.* **146**, 11371-11381 (2024).

3 Dong, H. *et al.* Green proton reservoirs of PANI for disposable high-performance zinc-ion batteries. *Nano Energy* **128**, 109768 (2024).

4 Xia, Z. *et al.* Tunable Ion Transport with Freestanding Vermiculite Membranes. *ACS Nano* **16**, 18266-18273 (2022).

5 Biao, J. *et al.* Inhibiting Formation and Reduction of Li_2CO_3 to LiC_x at Grain Boundaries in Garnet Electrolytes to Prevent Li Penetration. *Adv. Mater.* **35**, 2208951 (2023).

6 Asano, T. *et al.* Solid Halide Electrolytes with High Lithium-Ion Conductivity for Application in 4 V Class Bulk-Type All-Solid-State Batteries. *Adv. Mater.* **30**, 1803075 (2018).

7 Jin, Y. *et al.* Fluorinated $Li_{10}GeP_2S_{12}$ Enables Stable All-Solid-State Lithium Batteries. *Adv. Mater.* **35**, 2211047 (2023).

8 Li, X. *et al.* High-performance all-solid-state Li–Se batteries induced by sulfide electrolytes. *Energy Environ. Sci.* **11**, 2828-2832 (2018).

9 Zhao, Y. *et al.* Electron Percolating Shielded Interlayer Enabling Ultrastable All-Solid-State Lithium Metal Batteries. *Adv. Mater.* **38**, e15687 (2025).

10 Wu, X. *et al.* High-Conductivity Argyrodite Electrolyte with Self-Passivating Stability for Single-Electrolyte All-Solid-State Lithium Batteries. *Angew. Chem. Int. Edit.* **65**, e23225 (2026).

11 Zhao, F. *et al.* Anion sublattice design enables superionic conductivity in crystalline oxyhalides. *Science* **390**, 199-204 (2025).

12 Mi, J. *et al.* A ductile solid electrolyte interphase for solid-state batteries. *Nature* **647**, 86-92 (2025).

13 Guo, X. *et al.* A Stable Solid Polymer Electrolyte for Lithium Metal Battery with Electronically Conductive Fillers. *Angew. Chem. Int. Edit.* **62**, e202217538 (2023).

14 Shi, P. *et al.* A dielectric electrolyte composite with high lithium-ion conductivity for high-voltage solid-state lithium metal batteries. *Nat. Nanotechnol* **18**, 602-610 (2023).

15 Guo, S. *et al.* Dissociation mechanism of lithium salt by $BaTiO_3$ with spontaneous polarization. *Energy Environ. Sci.* **17**, 3797-3806 (2024).

16 Liu, X. *et al.* Dielectric $LiNbO_3$ electrolyte regulating internal electric field in composite solid-state electrolyte to fundamentally boost Li-ion transport. *Sci. China Mater.* **67**, 1947-1955 (2024).

17 Cheng, H. *et al.* Amorphous silicon nitride induced high dielectric constant toward long-life solid lithium metal battery. *Energy Storage Mater.* **53**, 305-314 (2022).

18 Wang, H. *et al.* Lithiated Copper Polyphthalocyanine with Extended π-Conjugation Induces LiF-Rich Solid Electrolyte Interphase toward Long-Life Solid-State Lithium-Metal Batteries. *Adv. Energy Mater.* **13**, 2204425 (2023).

19 Yang, L. *et al.* Identifying ultrathin dielectric nanosheets induced interface polarization for high-performance solid-state lithium metal batteries. *Energy Storage Mater.* **70**, 103473 (2024).

20 Kang, B.-H., Li, S.-F., Yang, J., Li, Z.-M. & Huang, Y.-F. Uniform Lithium Plating for Dendrite-Free Lithium Metal Batteries: Role of Dipolar Channels in Poly(vinylidene fluoride) and $PbZr_xTi_{1-x}O_3$ Interface. *ACS Nano* **17**, 14114-14122 (2023).

21 Yuan, Y. *et al.* Functional $LiTaO_3$ filler with tandem conductivity and ferroelectricity for PVDF-based composite solid-state electrolyte. *Energy Mater. Devices* **1**, 9370004 (2023).

22 An, X. *et al.* Giant dielectric ceramic of $Li_{0.3}Ti_{0.02}Ni_{0.68}O$ with abundant oxygen vacancies enabling high lithium-ion conductivity in composite solid-state electrolyte. *Carbon Neutrality* **3**, 22 (2024).

23 Yang, W. *et al.* Solvation-Tailored PVDF-Based Solid-State Electrolyte for High-Voltage Lithium Metal Batteries. *Angew. Chem. Int. Edit.* **63**, e202401428 (2024).

24 An, X. *et al.* Dielectric Filler-Induced Hybrid Interphase Enabling Robust Solid-State Li Metal Batteries at High Areal Capacity. *Adv. Mater.* **36**, 2311195 (2024).

25 Wu, Q. *et al.* Phase regulation enabling dense polymer-based composite electrolytes for solid-state lithium metal batteries. *Nat. Commun.* **14**, 6296 (2023).

26 Ma, Y. *et al.* Competitive Li-ion coordination for constructing a three-dimensional transport network to achieve ultra-high ionic conductivity of a composite solid-state electrolyte. *Energy Environ. Sci.* **17**, 8274-8283 (2024).

27 Wu, Y. *et al.* Fast Li^+ transport kinetics enabled by TiN nanofibers in hybrid polymer-based electrolytes for long-life Li metal batteries. *Energy Environ. Sci.* **18**, 2817-2825 (2025).

28 Zhang, W. *et al.* Single-phase local-high-concentration solid polymer electrolytes for lithium-metal batteries. *Nat. Energy* **9**, 386-400 (2024).

29 Yan, S. *et al.* Selectively fluorinated aromatic lithium salts regulate the solvation structure and interfacial chemistry for all-solid-state batteries. *Sci. Adv.* **11**, eads4014 (2025).

30 Lin, R. *et al.* Characterization of the structure and chemistry of the solid–electrolyte interface by cryo-EM leads to high-performance solid-state Li-metal batteries. *Nat. Nanotechnol* **17**, 768-776 (2022).

31 Ye, G. *et al.* All-Solid-State Lithium Metal Batteries with Microdomain-Regulated Polycationic Solid Electrolytes. *Adv. Mater.* **37**, 2417829 (2025).

32 Jin, Y. *et al.* Revealing the Influence of Electron Migration Inside Polymer Electrolyte on Li^+ Transport and Interphase Reconfiguration for Li Metal Batteries. *Angew. Chem. Int. Edit.* **63**, e202403661 (2024).

33 Sheng, B. *et al.* Sustained-Release PVDF-Based Electrolyte Producing LiF-Li_2O Layered Interphases for High-Rate Solid-State Lithium Metal Batteries. *Adv. Funct. Mater.* **36**, e14960 (2026).

34 Pei, F. *et al.* Interfacial self-healing polymer electrolytes for long-cycle solid-state lithium-sulfur batteries. *Nat. Commun.* **15**, 351 (2024).

35 Zhu, Y. *et al.* A locally solvent-tethered polymer electrolyte for long-life lithium metal batteries. *Nat. Commun.* **15**, 3914 (2024).

36 Peng, J. *et al.* Lithium Superionic Conductive Nanofiber-Reinforcing High-Performance Polymer Electrolytes for Solid-State Batteries. *J. Am. Chem. Soc.* **146**, 11897-11905 (2024).

37 Zhu, Y. *et al.* Uncoordinated chemistry enables highly conductive and stable electrolyte/filler interfaces for solid-state lithium–sulfur batteries. *Proc. Natl. Acad. Sci.* **120**, e2300197120 (2023).